Deep–Sea Research II 225 (2026) 105570

Contents lists available at ScienceDirect

Deep-Sea Research Part II

journal homepage: www.elsevier.com/locate/dsr2

Primary productivity and N_2-fixation in the eastern Indian ocean: Bottom-up support for an ecologically and economically important ecosystem

Sven A. Kranz[a,*], Jared M. Rose[b], Michael R. Stukel[c], Karen E. Selph[d], Natalia Yingling[c], Michael R. Landry[e]

[a] *Department of Biosciences, Rice University, Houston, TX, 77005, USA*
[b] *Marine Sciences Program and Department of Biological Sciences, University of South Carolina, Columbia, SC, 29208, USA*
[c] *Department of Earth, Ocean & Atmospheric Science, Florida State University, Tallahassee, FL, 32306, USA*
[d] *Department of Oceanography, University of Hawai'i at Manoa, Honolulu, HI, 96822, USA*
[e] *Scripps Institution of Oceanography, University of California at San Diego, La Jolla, CA, 92093, USA*

ABSTRACT

Oligotrophic ocean regions are characterized by strong nutrient limitation, low standing phytoplankton biomass, and highly efficient nutrient recycling. During the BLOOFINZ-IO expedition (February 2022), we quantified nutrient inventories, primary productivity and N_2 fixation in the Argo Basin of the eastern Indian Ocean, the sole known spawning ground for Southern Bluefin Tuna. Low concentrations of surface nitrate (<0.02 μmol L^{-1}) and persistent residual phosphate indicated N as the limiting macronutrient, with photophysiological indices consistent with iron colimitation. Depth-integrated net primary production (NPP), from ^{14}C-based *in-situ* incubations during 4 Lagrangian experiments, averaged ~460 mg C $m^{-2}d^{-1}$, generally agreeing with mean satellite-based NPP estimates (459 mg C $m^{-2}d^{-1}$) but with spatial discrepancies. Nitrogen fixation provided a consistent new nitrogen source, contributing ~16 % to local NPP in the upper euphotic zone. Gross primary production (GPP), from fast-repetition-rate-fluorometry-based estimates of electron transport, revealed significant autotrophic respiration losses, with mean GPP:NPP ratios of ~1.8 consistent with metabolic costs under nutrient limitation. Net community production (NCP) from O_2/Ar ratios averaged ~20 % of NPP in the upper 30 m. This result, in combination with N_2 fixation measurement, indicates that N_2 fixation supports most of the export production in the region. Together, the multi-method approach revealed a recycling-dominated ecosystem affected by episodic mixing events, where primary productivity is maintained primarily through efficient nitrogen recycling and physiological photoacclimation. These results provide a comprehensive baseline of bottom-up support of ecosystem productivity for the Argo Basin for assessing future climate-driven changes in stratification, nutrient cycling, and food-web dynamics.

1. Introduction

The eastern Indian Ocean, located between northwestern Australia and Indonesia and directly downstream of the Indonesian Throughflow, is a region of global significance for regulating heat transfer from the Pacific to the Indian Ocean (Lee et al., 2015; Desbruyères et al., 2017) and is the only known spawning region for Southern Bluefin Tuna (SBT) (Farley and Davis, 1998). However, it remains a sparsely studied area regarding its ecological and biogeochemical processes. The BLOOFINZ (Bluefin Larvae in Oligotrophic Ocean Foodwebs, Investigations of Nutrients to Zooplankton) project investigated the region during the peak SBT spawning season in January–February 2022 to assess its potential vulnerabilities to future climate change. Quantification of gross-, net- and net community-productivity and its support by nitrogen (N) sources are central to understanding the energy available for higher trophic levels. In the present study, we focus on primary production, N_2 fixation and associated photophysiologial measurements conducted during four multi-day Lagrangian experiments.

Despite low rates of production per unit area, oligotrophic systems contribute an estimated 30–40 % of total global marine primary production (Behrenfeld and Falkowski, 1997; Field et al., 1998). Primary productivity depends on efficient recycling of N through ammonification (Dugdale and Goering, 1967), and N_2 fixation can play a significant role in supporting new production (Raes et al., 2015; Tang et al., 2019). In these systems, only a small fraction of primary production is usually exported out of the euphotic zone (Buesseler et al., 1998; Henson et al., 2019). Deep chlorophyll maxima (DCM), where a substantial portion of the phytoplankton community resides, still pose some challenges for

---

This article is part of a special issue entitled: BLOOFINZ/INDITUN published in Deep-Sea Research Part II.

* Corresponding author.

E-mail address: sk235@rice.edu (S.A. Kranz).

https://doi.org/10.1016/j.dsr2.2025.105570
Received 30 June 2025; Received in revised form 12 November 2025; Accepted 22 November 2025

satellite-based net primary production (NPP) algorythms. Though algorythmns by Westberry et al. (2008) do account for vertical chlorophyll distribution, productivity estimate and their dynamics, especially under nurtrient stress, still require field verification. Questions thus arise on how general algorithms in these oligotrophic region relate to depth-resolved measurements of NPP from ^{14}C uptake or to high-resolution quantification of gross primary (GPP) and net community productivity (NCP) (Robinson et al., 2009; Quay et al., 2010; Hamme et al., 2012; Schuback et al., 2015; Teeter et al., 2018; Kranz et al., 2020).

In this study, we applied a multi-method approach to quantify nutrients, productivity metrics and N_2 fixation in SBT spawning waters overlying the 5000-m deep Argo Abyssal Plain (hereafter, Argo Basin) off NW Australia (Fig. 1). We directly compare NPP assessments from *in situ* incubations and satellite products for four multi-day Lagrangian experiments. From continuous surface measurements of O_2:Ar, Fast Repetition Rate Fluorometry (FRRf) and photophysiological parameters in transect sampling across the basin, we derive carbon-based estimates of NCP, GPP and production relationships. From direct experimental measurements of N_2 fixation rates, we establish that diazotrophy is the main contributor to the new N required to balance the measured (Stukel et al., this issue) export fluxes. Our overall goals were to evaluate the magnitude and variability of autotrophic production and N supply to this key region during the peak SBT spawning season (austral summer) and to establish baseline metrics for understanding future responses of the system to climate change. Please note that this article is part of an end-to-end, interdisciplinary study of the southern bluefin tuna spawning region, linking physics, chemistry, and biology to uncover the drivers of productivity and nutrient–carbon cycling in this ecologically and economically important ecosystem (please see Landry et al. (This issue) for an overview article. Throughout the article, we reference our more detailed companion papers directly connection to this article.

1.1. General sampling plan

The Argo Basin was sampled on BLOOFINZ cruise RR2201 of *R/V Roger Revelle* between 31 January and March 3, 2022 (Fig. 1). We first conducted an east-to-west transect across the central basin, then sampled south to begin the first of four Lagrangian experime Radke et al. (2017) nts (hereafter, "cycles") in the southern basin. Following the cycle experiments, two additional transects were sampled before departing the basin, first east-to-west at 15°S, then west-to-east at 13.5°S. During each cycle, sampling and incubations were done on a repeated daily schedule for 3–5 days following a satellite-tracked drifter with a 3-m drogue centered at 15-m depth (Landry et al., 2009; Stukel et al., 2015). Seawater samples for nutrients, phytoplankton and experimental incubations were collected with a 12-place CTD rosette of 10-L Niskin bottles. Incident Photosynthetically Active Radiation (PAR) was measured continuously by the ship's meteorological system and a PAR sensor on CTD profiles. During both transect and cycle experiments, continuous measurements of mixed-layer O_2:Ar ratios, fluorometric chlorophyll *a* (Chl*a*) and FRRf were taken by instruments plumbed into the ship's seawater intake delivered at ~4 L min^{-1} by a diaphragm pump (Graco Husky 1050e).

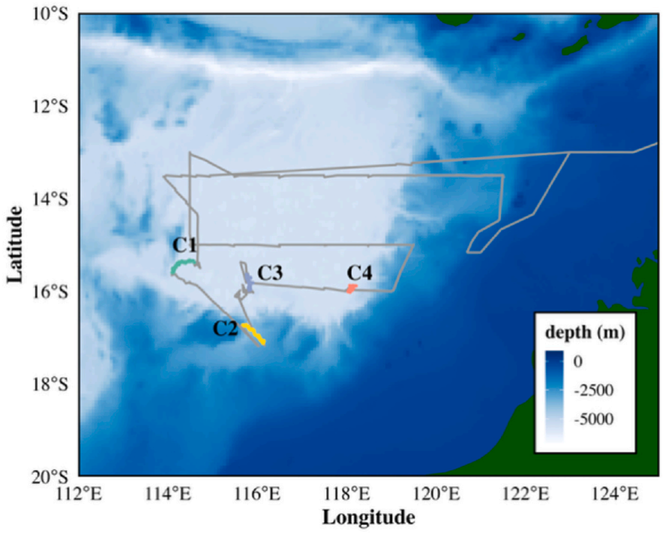

Fig. 1. Map of the study area as a bathymetry with cruise track (in grey) and cycle location (in colors). (For interpretation of the references to color in this figure legend, the reader is referred to the Web version of this article.)

Water samples for extracted Chl*a* analyses were taken from CTD profiles, filtered onto GF/F filters, extracted in 90 % acetone for 24 h and measured with a 10AU fluorometer (Turner Designs). Surface Chl*a* values were also continuously measured by a fluorometer. However, underway data between February 14 and 23 was unusable due to biofouling. Nutrient samples (50 mL) were filtered directly from CTD bottles through acid-cleaned 0.2-μm Acropak in-line capsules (Pall-Gelman) into 3X-rinsed Nalgene HDPE bottles and immediately frozen at −20 °C. Concentrations of nitrate, nitrite, ammonium, phosphate and silicate concentrations were measured with a Seal AutoAnalyzer 3 at the Scripps Institution of Oceanography Data Facility.

1.2. Net primary productivity (NPP) on in-situ array and satellite derived NPP

Net primary production was measured by ^{14}C-bicarbonate uptake (NPP_{14C}) in *in-situ* incubations following Morrow et al. (2018). For each cycle day, water was collected at six depths spanning the euphotic zone on the 02:00 (local) CTD cast and transferred gently via silicon tubing into acid-washed 280-mL polycarbonate incubation bottles that had been pre-soaked with Milli-Q water and rinsed three times with station water. For each depth, three replicate bottles and one dark bottle were spiked with 10 μCi $H^{14}CO_3^-$ and incubated for 24 h (beginning at 04:00 local) in mesh bags attached at the collection depth. Following incubation, samples were processed under dim red light. After a subsample (100 μL) was taken for total radioactivity, bottle volumes were filtered onto GF/F filters, acidified with 0.5 mL of 10 % biological-grade HCl, and degassed for 24 h. The filters were subsequently placed into scintillation cocktail and analyzed with a liquid scintillation counter. NPP_{14C} was calculated according to (Steemann Nielsen, 1952) as:

$$NPP_{14C}\ (\mu g\ C\ L^{-1}\ d^{-1}) = ((As - Ab)\ /\ At) \times DIC \times 1.05 \times (1/t))\ (Eq.\ 1)$$

where As = sample activity; Ab = blank activity; At = total bottle activity; DIC = dissolved inorganic carbon (25.5 μmol C L^{-1}); and t = incubation time (1 day). Depth integrations were done in RStudio by trapezoidal interpolation to 30 m and to the deepest sample measurement. We assumed that rates measured at our shallowest depth (5m) were indicative of rates from the surface to 5 m, in order to integrate productivity thoughout the water column.

NPP_{Sat} was also estimated for the Argo region from 8-day composite NPP satellite data products of the CAFÉ model from Oregon State University (Silsbe et al., 2016). Satellite based estimates of NPP for the region had been described by Kehinde et al. (2023). Here, we re-analyzed the data along the cruise track using the CAFÉ algorithm which we think captures the productivity in this region best. We also focus specifically on the Lagrangian cycles and averaging the data over 1-min intervals based on the ship's location rather than the larger ITF productivity assessment of (Kehinde et al., 2023).

1.3. N_2 fixation on in-situ array

N_2 fixation rates were measured using the $^{15}N_2$ gas tracer technique following the bubble dissolution method described by (Mohr et al., 2010a). Because of the extra setup time required, samples for these incubations were taken from the 22:00 CTD and thus differed from 02:00 (local) productivity samples, though were taken in close proximity to the drift array and assumed to have a similar plankton composition. For each of 6 depths, unfiltered seawater was directly transferred into triplicate acid cleaned 4.6 L polycarbonate bottles and kept in the dark until spiked with $^{15}N_2$-containing water. To improve dissolution of $^{15}N_2$ into the spiked inoculum, 1.2 L of the same water was degassed (Mohr et al., 2010a) using a Pfeiffer vacuum pump and rigorously stirred with Teflon-coated stir bar. The partially degassed water was transferred by peristaltic pump into a 1 L tedlar gas sampling bag (Restek) with residual dissolved O_2 measured during transfer with an optode system (Firesting, Germany). On average, 35 % of O_2 was retained indicating a similar residual $^{14}N_2$. The bags were filled with 1.2 L degassed seawater, spiked with 35 ml of $^{15}N_2$ gas (98–99 atom %, Cambridge Isotope Laboratories), and transferred to a automatic bubble disturbing setup which moved the bubble continuously for ~1.5 h. The $^{15}N_2$ enrichment of this inoculum was calculated to be ~50 %. Around 03:00, an hour before array deployment, ~350 ml of the inoculum was added to each of three 4.6-L bottles, and the bottles were filled to capacity with natural seawater for a final $^{15}N_2$ enrichment of around 7.5 %. These bottles were subsequently incubated for 24 h on the *in-situ* array.

Post incubation, aliquots from each bottle were transferred into 50–125 ml serum bottles using a peristaltic pump, and 5–12 μl of HgCl was added to kill biological activity. These bottles were sealed with Teflon-coated septums for gas-tight seals and stored in the dark at room temperature. Residual water from the incubations was filtered onto precombusted GF/F under dim light, and filters were frozen at −20 °C before being dried in a desiccator and packed into tin cups for analysis at the Stable Isotope Laboratory. The $^{15}N_2$ spike concentration was measured on shipboard with a Pfeiffer QMS 220 MIMS system. A long needle inserted into the serum bottle was connected by a microvolume gear pump to the membrane system (Bay Instruments), and the ^{15}N:^{14}N gas ratio was measured and found to average 5.7 % (slightly less than theoretically assumed). N_2 fixation was calculated according to (White et al., 2020). Depth integrations were done in RStudio by trapezoidal interpolation to 30 m and to the deepest sample measurement at each cycle day (max. 90 m).

1.4. Net Community Production (NCP)

NCP estimates from O_2:Ar measurements reflect oxygen production by photoautotrophs, respiration by photo- and heterotrophs, and corrections for physical gas exchange processes assuming steady-state processes over the residence time of O_2 (Craig and Hayward, 1987). Continuous underway measurements of O_2:Ar were obtained by equilibrium inlet mass spectrometry (EIMS, Pfeiffer QMS 220) as described by Kranz et al. (2020). Biological supersaturation of oxygen (ΔO_2:Ar) was determined by normalizing the measured O_2:Ar ratio to values obtained during regular (~1 h every 8 h) calibrations with atmosphere-equilibrated seawater. Data were smoothed by 5-min running averaging, and calibration times were exchanged with correlated extrapolations of the prior and post calibration data. NCP rates were calculated as:

$$\mathrm{NCP} = \mathrm{k} \cdot \Delta(\mathrm{O_2} / \mathrm{Ar})[\mathrm{O_2}]_{\mathrm{sol}} \rho \qquad \text{(Eq. 2)}$$

where k is the piston velocity for O_2 gas exchange (k; m d^{-1}) estimated from the square of satellite-measured wind speed and the temperature-dependent Schmidt number (Sc) for O_2 (Wanninkhof, 2014). To incorporate the temporal dynamics of wind forcing and upper-ocean mixing, a time-weighted mean k was computed by incorporating the wind speed history and mixed-layer depth (MLD) (Reuer et al., 2007). $[O_2]_{sol}$ is the mixed-layer oxygen solubility, and ρ is the average ML density. $\Delta(O_2 / Ar)$ is the biological oxygen signal defined by $\Delta(O_2 / Ar) = \frac{(O_2/Ar\ )}{(O_2/Ar)_{cal}} - 1$.

NCP was calculated for two estimates of mixed layer depths ($MLD_{\sigma\theta}$ and MLD_{O2}) and also at a constant depth of 30 m. $MLD_{\sigma\theta}$ was determined from CTD profiles as the depth at which the density had increased by 0.01 kg m^{-3} relative to the density at 5 m. We also calculated MLD_{O2} as a 2 % change in O_2 concentration from a reference depth of 10 m (Castro-Morales and Kaiser, 2012). Both MLD estimates were smoothed by 3-d running means prior to the ventilation calculation to account for internal waves and other variations. Among our three approaches, $NCP_{\sigma\theta}$ and NCP_{O2} are dynamic estimates constrained by hydrographic (σ_θ) and hydrographic/biological (O_2) structures of the water column, whereas NCP_{30m} provides a fixed-depth reference for comparing between methods (GPP only valid above 30 m, NPP valid for full water column but with limited sample size within shallow mixed layers (e.g., <10-m MLDσ_θ). NCP was calculated as mmol O_2 m^{-2} d^{-1} and converted to NCP_C (mg C m^{-2} d^{-1}) using a photosynthetic quotient of 1.3 and 12.01 g mol^{-1} for carbon. We adopted PQ = 1.3, instead of the ~1.1 expected for NH_4^+ utilization, to account for Fe-stress-induced alternative electron flows (e.g., cyclic and Mehler pathways, photorespiration) that decouple O_2 evolution from CO_2 fixation and increase the apparent PQ (Laws, 1991; Behrenfeld and Milligan, 2013).

1.5. Gross primary productivity and photophysiology using FRRf

Gross primary productivity (GPP) was estimated using Fast Repetition Rate fluorometry (FRRf) based on Oxborough et al. (2012) and adapted for field applications following Schuback et al. (2015, 2016). Implementation of the method for this study closely followed Kranz et al. (2020). The method applied is based on single turnover excitement of the photosystem, measured as photosystem II fluorescence (Oxborough et al., 2012; Schuback et al., 2015; Boatman et al., 2019; Kranz et al., 2020). The FRRf data provide estimates of gross primary production expressed in electrons per photosystem II reaction center.

Shipboard measurements were made from the ship's seawater system using a bench-top FastAct 2+ Fast TRAKA instrument (Chelsea, UK). Photosynthesis versus irradiance (P vs. E) curves were run on a ~30-min sampling interval using single-turnover flash sequences to resolve photosystem II (PSII) photophysiological parameters. For every 5-ml sample, water was first purged through the cuvette to remove old sample and acclimated to low light (12 μmol photons m^2 s^{-1}) for 10 min, then dark acclimated for 60 s. Measured parameters included the dark/low light adapted maximum quantum yield of PSII (Fv/Fm), the functional absorption cross-section of PSII (σPSII), and the effective quantum yield under ambient light (Fq/Fm'). Additional photophysiological parameters are described in Supplemental Table 1.

Using a modified version of the absorbance algorithm (Oxborough et al., 2012), volume-based productivity rates (i.e., mol electrons $(RCII)^{-1}$ m^{-3} d^{-1}) were calculated as:

$$JV_{PSII,abs} = \Phi_{RCII} \cdot F'_o \cdot K_a \cdot E \cdot 8.64 \times 10^{-8} \qquad \text{(Eq. 3)}$$

where $F'_o = (F_m \cdot F_0)/(F_m - F_0) \cdot \left(F'_q / F_m\right)$; K_a is the instrument calibration factor (11800 m^{-1}); E = irradiance (μmol photons m^{-2} s^{-1}) of actinic light in the instrument and the factor 8.64 x 10^{-8} converts μmol photons m^{-2} s^{-1} to mol photons m^{-2} d^{-1} and kg to mg. The photon to electron conversion Φ_{RCII} (mol e^- mol $photon^{-1}$) has a constant value of 1, representing one electron transferred from P680 to quinone A (Q_A) for each photon absorbed and delivered to reaction center RCII (Kolber and Falkowski, 1993). RCII was estimated as:

$$RCII = K_a \cdot F_0 /_{\sigma_{PSII}} \qquad \text{(Eq. 4)}$$

where F_0 is dark-adapted base fluorescence and σ_{PSII} is the absorption cross-section area of the dark-adapted photosystem. Here, we used mean nighttime σ_{PSII} measurements and assumed similar absorption cross section during the following day to avoid errors from daytime suppression due to enhanced base fluorescence and non-photochemical quenching. JV_{PSII} (mol electrons m^{-3} d^{-1}) was converted to carbon units by the factor Φe:c (Schuback and Tortell, 2019):

$$\Phi_{e:C} / \eta_{RCII} = 486 \cdot NPQ_{NSV} + 1854 \quad \text{(Eq. 5)}$$

where $\Phi_{e:C}$ is the electron to carbon fixation ratio, η_{RCII} is the RCII to Chl-*a* ratio, and NPQ_{NSV} is the normalized Stern-Volmer non-photochemical quenching coefficient. η_{RCII} was determined using the RCII calculated in Eq. (4) and dividing by Chl*a* concentration from the ship's fluorometer. During the timespan where the fluorometer readings were faulty, we used nighttime F_0 from the FRRf and the relationship between F_0 and Chl*a* before the sensor was fouled.

To calculate water column GPP from FRRf measurements, we used *in-situ* light attenuation from noon CTD profiles to calculate the light field over the diurnal cycle. P vs. E relationships were determined from FRRf productivity parameters according to (Platt et al., 1980) if photoinhibition was observed (Eq. (6)) or from Webb et al. (1974) if no photoinhibition was observed (Eq. (7)):

$$Productivity = Ps \times \left[1 - e^{\frac{-\alpha \times E}{Ps}}\right] \times e^{\frac{-\beta \times E}{Ps}} \quad \text{(Eq. 6)}$$

$$Productivity = Ps \times \left[1 - e^{\frac{-\alpha \times E}{Ps}}\right] \quad \text{(Eq. 7)}$$

where *Ps* is the maximum photosynthesis, E is PAR, α is the initial photosynthesis slope under low irradiance, and β is the slope under high/stressful irradiance.

Due to system oligotrophy, some measurements did not pass quality control even at lower light (250 μmol photons m^{-2} s^{-1}). These P vs. E curves were omitted from further analysis, but the parameters were used for mean estimates of basic dark adapted photophysiological parameters (see below). Due to instrument failures and missing data, we obtained a higher temporal resolution of GPP by averaging the valid daytime productivity estimates (Eq. (6) and (7)) for every 30 min at their respective light conditions. We considered the parameters only valid to 30 m depth because cellular Chl*a* changed below 30 m (Supplemental Fig. 3). Additional photophysiological parameters derived from dark-adapted measurements are described in Supplemental Table S1.

1.6. Statistical methods

All statistical analyses were conducted in R (version 2024.12.0 + 467; R Core Team). For comparisons of productivity metrics across cycles and treatments, we assumed normality and homogeneity. Significant differences among Lagrangian cycles were tested by one-way ANOVA followed by post-hoc pairwise comparisons by Tukey's Honest Significant Difference (HSD) test. Depth-integrated rates (e.g., ^{14}C-NPP, GPP, N_2 fixation) were calculated by trapezoidal integration of depth profiles over the upper 30 m and the full photic zone, with variability reported as standard error of the means (SEM) of replicate profiles. All plots were generated using ggplot2, and compositing of multi-panel figures was performed using patchwork packages. The significance level was set at α = 0.05 for all tests.

2. Results

2.1. Environmental properties

During cruise RR2201, the Argo Basin was characterized by warm surface waters and strong thermal stratification (Fig. 2A, Table 1). Sea surface temperatures (upper 30 m) ranged from ~28 °C to 30 °C across all cycles. Subsurface temperatures at the DCM (67–75 m) were ~4 °C lower compared to surface values, indicating strong thermal stratification. Salinity remained relatively uniform throughout the surface layer in Cycles 1, 2, and 4 (hereafter C1 to C4), with modest increases at depth (Fig. 1 B). The highest salinity was observed during Cycle 2, while Cycle 3 showed a distinct salinity anomaly near 50 m depth, suggesting a subsurface intrusion of water from lateral advection or a remnant signal from a prior mixing event. Mixed layer depth (Fig. S2, Table 1), based on sigma theta was determined to average around 30.5 ± 3.1, 9.4 ± 1.0, 6.6 ± 0.2 and 9.2 ± 0.8 for C1 to C4, respectively. Mixed layer depths based on the oxygen profiles for analysis of the O_2/Ar data (MLD_{O2}) were determined to be 53 ± 7, 32 ± 7, 17 ± 2.5, 20.5 ± 7 m for C1 to C4, respectively (Fig. S2, Table 1). The generally deeper mixing during C1 was the result of a storm system which passed through the area shortly before C1. Since C3 was the same water mass as C1, restratification occurred within 7 days. $MLD_{\sigma\theta}$ based on density was consistently shallower than $MLD_{\sigma\theta}$, particularly during stratified periods (Table 1). These discrepancies reflect the differing time scales of physical mixing (hours to days) and biological and air-sea gas exchange processes (days to weeks), the latter being more appropriate for the O_2/Ar NCP assessment.

Nutrient concentration profiles verified the oligotrophic nature of the basin (Fig. 2, Table 1). Nitrate concentrations (NO_3^-) were generally depleted (Fig. 2F), averaging (±SEM) 0.018 ± 0.04 μM in surface waters down to 50 m, with nitraclines (the depth at which nitrate

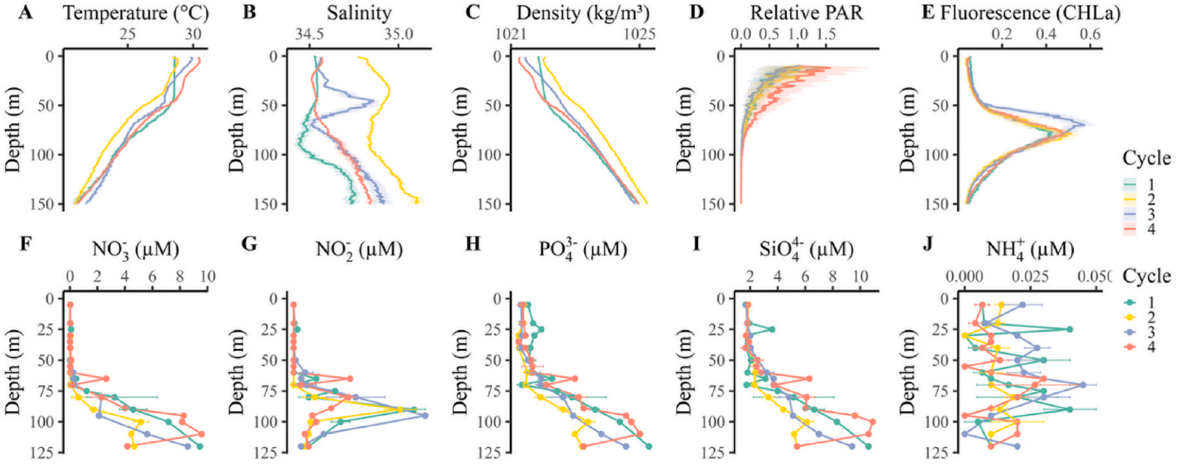

Fig. 2. Physical and biochemical and profiles from the 4 cycles plotted to 150-m depth. A) Temperature (°C), B) Salinity (PSU), C) Density (kg m^{-3}), D) Relative PAR (μmol photons m^{-2} s^{-1}), E) Chl*a* fluorescence (μg L^{-1}) taken from the CTD rosette depth profiles and plotted as average per cycle with 95 % confidence interval (shaded area). F-J) Nutrient profiles (μM) taken from CTD niskin bottles. F) NO_3^-, G) NO_2^-, H) PO_4^{3-}, I) SiO_4^{4-} J) NH_4^+. Error bars denote standard deviation when multiple samples were taken from the same depth during a cycle.

Table 1
Nutrient and biophysiochemical parameters during the cyles, averaged by depth intervals. Where shown, the errors are 1 standard error of the mean.

	Depth	Cycle 1	Cycle 2	Cycle 3	Cycle 4
Starting Dates		02/04	02/09	02/15	02/20
Par	0–30 m	75.80 ± 4.15	161.25 ± 7.37	156.61 ± 7.52	102.63 ± 5.38
	30–50 m	24.42 ± 1.37	53.46 ± 2.85	53.77 ± 3.05	48.39 ± 2.86
	50–100 m	6.35 ± 0.28	11.52 ± 0.54	10.44 ± 0.52	11.84 ± 0.61
	Deep	0.17	0.17 ± 0.01	0.15	0.13 ± 0.01
Salinity	0–30 m	34.54	34.85	34.57	34.54
	30–50 m	34.54	34.89	34.71	34.54
	50–100 m	34.48	34.83	34.62	34.60
	Deep	34.69	35.02	34.82	34.78
Temp	0–30 m	28.57	28.41 ± 0.01	29.08 ± 0.01	29.78 ± 0.01
	30–50 m	28.49 ± 0.01	27.35 ± 0.03	27.87 ± 0.01	28.80 ± 0.02
	50–100 m	26.06 ± 0.03	24.53 ± 0.02	25.40 ± 0.02	25.73 ± 0.02
	Deep	12.96 ± 0.08	16.12 ± 0.06	14.45 ± 0.08	14.49 ± 0.07
$MLD_{\sigma\theta}$		41 ± 15	10 ± 5	6.8 ± 1.2	10.76 ± 3.7
MLD_{O2}		53 ± 7	32 ± 7	17 ± 2.5	20.5 ± 7
NO_3^-	0–30 m	0.03 ± 0.01	0.02	0.01	0.01
	30–50 m	0.01	0.02 ± 0.01	0.05 ± 0.03	0.01
	50–100 m	1.94 ± 0.75	1.33 ± 0.45	1.14 ± 0.46	2.10 ± 0.91
	Deep	21.03 ± 3.90	11.92 ± 2.22	20.02 ± 3.04	13.56 ± 1.83
NH_4^+	0–30 m	0.01	0.01	0.01	0.01
	30–50 m	0.01 ± 0.01	0.01	0.02	0.01
	50–100 m	0.02	0.02	0.02	0.01
	Deep	0.01	0.01	0.01	0.01
PO_4^{3-}	0–30 m	0.11 ± 0.01	0.05 ± 0.01	0.05	0.06 ± 0.02
	30–50 m	0.10 ± 0.01	0.04	0.06 ± 0.01	0.08 ± 0.02
	50–100 m	0.24 ± 0.05	0.20 ± 0.03	0.20 ± 0.04	0.30 ± 0.06
	Deep	1.55 ± 0.27	0.85 ± 0.14	1.45 ± 0.21	0.95 ± 0.12
NO_2^-	0–30 m	ND	ND	ND	ND
	30–50 m	ND	ND	ND	ND
	50–100 m	0.07 ± 0.02	0.08 ± 0.03	0.07 ± 0.03	0.07 ± 0.02
	Deep	0.03 ± 0.01	0.02	0.01 ± 0.01	0.01 ± 0.01
SiO_4	0–30 m	2.00 ± 0.22	1.85 ± 0.02	1.79 ± 0.04	1.77 ± 0.02
	30–50 m	1.80 ± 0.08	1.97 ± 0.05	2.13 ± 0.08	2.02 ± 0.39
	50–100 m	3.85 ± 0.70	3.71 ± 0.33	4.13 ± 0.48	5.00 ± 0.77
	Deep	44.31 ± 13.22	17.37 ± 5.31	40.23 ± 10.29	16.16 ± 2.81

concentrations first exceeded 1 μmol L^{-1}) around 65–81 m. Phosphorus (Fig. 2H), showed a remaining concentration of 0.07 ± 0.02 μM PO_4^{3-} μM. P* (the overabundance of phosphorus relative to nitrogen $P^* = [PO_4^{3-}] - 16/[NO_3^-]$) averaged 0.06 in the upper 50 m and 0.1 for the upper 100 m (Figure Supplemental 2), indicating that nitrate was a limiting major macro-nutrient in the surface ocean. Silicic acid (Fig. 1H) was measured at average concentrations of 1.89 ± 0.04 μM within the upper 50 m; ammonia (NH_4^+) was barely measurable (0.012 ± 1 μM) throughout the water column (Fig. 1I), indicating active recycling. Nitrite (Fig. 1G) had a prominent maximum, indicating enhanced nitrification, slightly below the deep chlorophyl maximum (DCM) (Fig. 1E). The DCM (Fig. 1E) depths ranged from 67 to 75 m, with the nitracline typically slightly deeper than the DCM. The euphotic zone (EZ) depth (1 % surface PAR) (Fig. 1D) was slightly deeper than the DCM, while subsurface fluorescence peaks marked the DCM and associated productivity zones.

2.2. Net primary productivity (NPP) on in-situ array

^{14}C-based NPP profiles showed distinct differences across the four Lagrangian experiments. For C1, NPP_{14C} was greatly reduced in the lower euphotic zone (EZ) compared to the surface (~78 % reduction at 50 m) (Fig. 3A) due to low light (cloud cover) during the first 3 days (Fig. S3), but the rates increased sharply on day 4. with 50-m NPP being 8 % higher than the surface (Fig. 3A). For C2 and C3 (Fig. 3B and C), profiles were relatively constant to 60 m. In contrast, C4 (Fig. 3D) showed a strong decrease in the upper 20 m followed by an almost linear decrease with deeper depth, which correlated with increasing cellular Chl*a* below 40 m (see Fig. S1).

Integrated NPP_{14C} rates were relatively consistent across the cycles except for days 1–3 of C1. Cycle-averaged productivity was lowest in C1 (283 ± 72 mg C m^{-2} d^{-1}), and C2-C4 exhibited higher full-depth integrated NPP_{14C} values of 542 ± 43, 546 ± 53, and 496 ± 28 mg C m^{-2} d^{-1}, respectively. The overall mean NPP_{14C} across all four cycles was 460 ± 40 mg C m^{-2} d^{-1}. Integrated ^{14}C-based primary productivity for the upper 30 m (the habitat depth of SBT larvae) (Fig. 2E insert, Table 2) averaged roughly half of the full EZ-integrated rates. Cycle mean values ranged from 164 ± 20 mg C m^{-2} d^{-1} in C1 to 240 ± 21 mg C m^{-2} d^{-1} in C4, with an overall average of 212 ± 14 mg C m^{-2} d^{-1}.

Supplementing our direct NPP_{14C} measurements, NPP_{Sat} estimates for the region averaged 450 mg C m^{-2} d^{-1} along the cruise track (Fig. 3). Productivity was highest in patches in the shelf area between 120 and 125°E and along the Australian coastline south of Argo Basin. West of 120 °E, productivity between 12.5 and 17.5°S was relatively uniform (464 mg C m^{-2} d^{-1} on average), showing no obvious indications of local production hot spots in the Argo Basin during our cruise (Fig. 3).

For the Lagrangian cycles, 8-day NPP_{Sat} estimates ranged from 428 to 518 mg C m^{-2} d^{-1} (Table 2)Fig. 4), with an overall cycle mean of 459 ± 2 mg C m^{-2}. Post-hoc Tukey's HSD tests indicated significant differences among cycles. During C1, mean NPP_{Sat} (515 mg C m^{-2} d^{-1}) was significantly higher than C2-C4 ($p < 0.01$). In C2, productivity was lowest (446 ± 19 mg C m^{-2} d^{-1}; $p = 0.002$ versus C1) and exhibited the highest variability. NPP_{Sat} for C3 (Feb. 19–26; 429 ± 1 mg C m^{-2} d^{-1}) was significantly lower than both C1 ($p < 0.001$) and C4 (459 ± 2 mg C m^{-2} d^{-1}; $p = 0.03$).

2.3. N_2 fixation on in-situ array

N_2-fixation rates are unavailable for C1 and the first two days of C2 due to lost samples. Measured rates ranged generally from 10 to 20 nmol N_2 L^{-1} d^{-1} with an average of ~15 nmol N_2 L^{-1} d^{-1} for the upper 60 m, decreasing sharply to 1–2 nmol N_2 L^{-1} d^{-1} at depths of 70–80 m in the nitracline. Based on Redfield stoichiometric conversion to mg C m^{-2} d^{-1}, EZ-integrated rates ranged from 60 to 86 mg C m^{-2} d^{-1}, with the highest value on day 3 of C3 (84 ± 4 mg C m^{-2} d^{-1}) and the lowest on day 3 of C4 (57 ± 3 mg C m^{-2} d^{-1}) (Fig. 5, Table 2). Corresponding 30-m integrated rates ranged from 27 ± 6 to 41 ± 0 mg C m^{-2} d^{-1}, averaging 34 ± 2 mg C m^{-2} d^{-1}. N_2-fixation for the full depth was highest during C2 (84 ± 3 mg C m^{-2} d^{-1}), followed by C3 (76 ± 7 mg C m^{-2} d^{-1}) and C4 (61 ± 4 mg C m^{-2} d^{-1}), giving an overall average of 74 ± 3 mg C m^{-2} d^{-1} (Table 2).

2.4. Gross primary productivity (GPP)

Due to low biomass, about 30 % of the P vs E curves did not pass

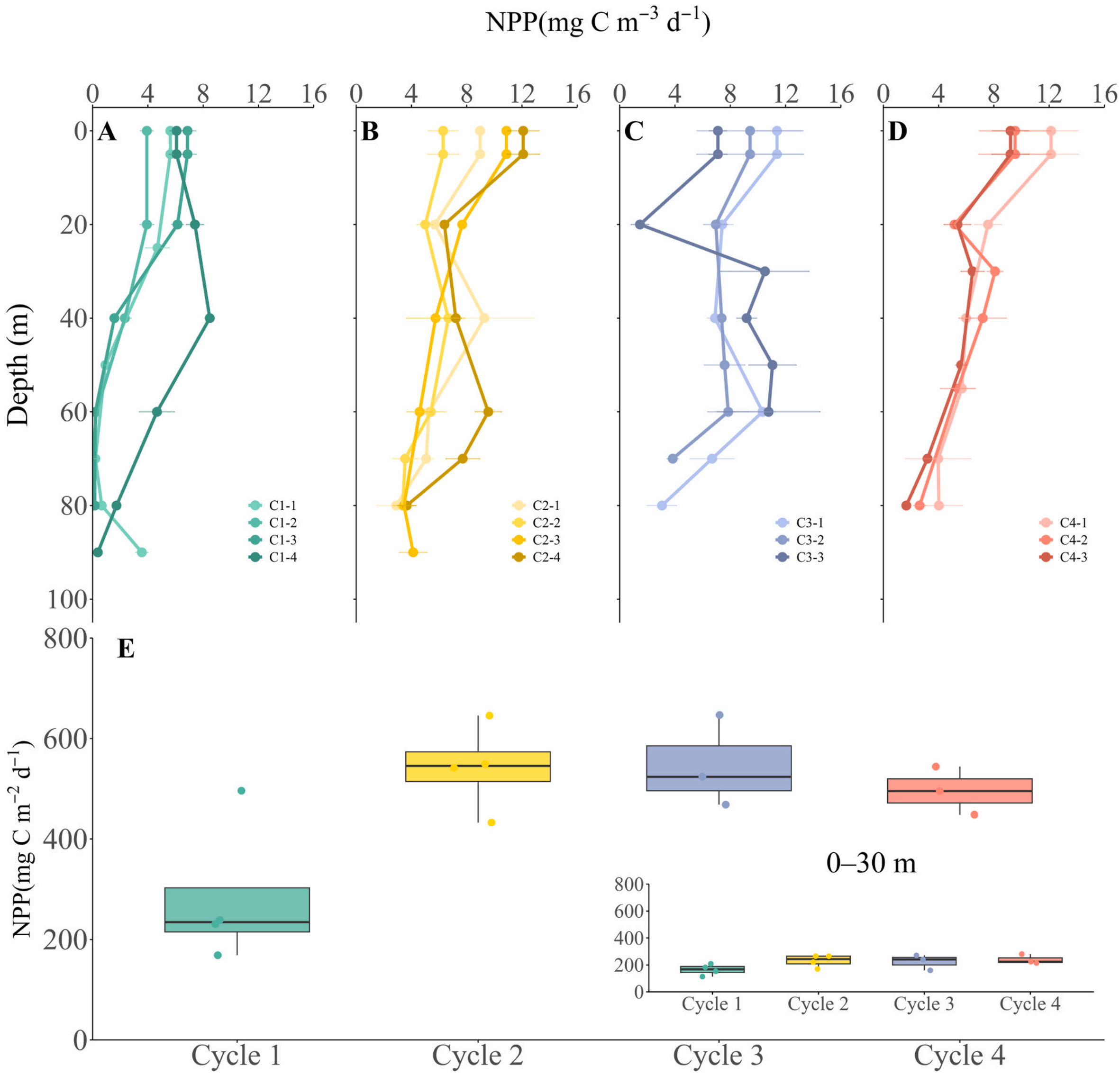

Fig. 3. Daily measurement profiles and integrated values of ^{14}C based net primary productivity (NPP_{14C}). A-D) NPP_{14C} profiles for all cycles and cycle days with error bars denoting 1 standard error of the mean. E) Integrated productivity in mg C m^{-2} d^{-1}. Dots indicate the water column productivity for each day (n = 4, 4, 3, and 3 for Cycles 1, 2, 3, and 4, respectively) while the boxplot indicates the median and interquartile range of integrated values. Insert: Depth integrated NPP_{14C} of the water column of the upper 30 m.

quality control (i.e. low signal-to-noise ratio resulted in low data confidence at light levels >250 μmol photons m^{-2} s^{-1}). Because community compositions (Selph et al.,; Yingling et al.,) and base GPP calculation parameters were similar among cycles (Fig. S3), we used the diurnal average of the fitted photosynthetic parameters (α, P_{max}, β) from the P vs. E equations to substitute for missing data (see methods, Eq. (6) and (7)). These data (Fig. 6A–D), revealed a midday productivity saturation for most cycles (e.g., flat production despite the sinusoidal solar cycle).

FRRf-based estimates of gross primary productivity for the upper 30 m (GPP_{30m}) varied daily from 188 to 465 mg C m^{-2} d^{-1}, with a cycle average of 345 ± 16 mg C m^{-2} d^{-1} (Fig. 6E–Table 2, Table S2). Despite reduced PAR at the beginning, C1 showed similar GPP rates compared to the other cycles (mean 352 ± 23 mg C m^{-2} d^{-1}), with daily values from 305 to 403 mg C m^{-2} d^{-1} (Table S2). C2 showed day-to-day variability (217–465 mg C m^{-2} d^{-1}) and a similar mean value (345 ± 55 mg C m^{-2} d^{-1}) comparable to C1. C3 had the highest mean GPP_{30m} at 381 ± 80 mg C m^{-2} d^{-1}, peaking at 715 mg C m^{-2} d^{-1} with an integrated daily rate of 513 ± 31 mg C m^{-2} d^{-1} on day 3, yet these mean data were not significantly different compared to C1 and C2. C4 displayed the lowest GPP_{30m}, ranging from 188 to 375 mg C m^{-2} d^{-1} with a cycle mean of 302 ± 57 mg C m^{-2} d^{-1}. Despite these cycle differences, a one-way ANOVA using daily GPP_{30m} revealed no statistically significant differences among cycles ($p > 0.05$). Direct comparison of GPP_{30m} to NPP_{14C} for the upper 30 m resulted in a mean gross-to-net productivity ratio ($GPP:NPP_{30m}$) of 1.63 ± 0.14 (Table 2) with high variability in individual daily estimates from 0.67 to 3.21 (Table S2).

2.5. Net community productivity (NCP)

Net community productivity was calculated based on O_2:Ar data, wind velocity and mixed layer depth. $MLD_{\sigma\theta}$ estimates for C2 to C4 were below 10 m, while O_2 profiles indicated a deeper MLD (Fig. S2). Hence, we analyzed NCP based on both $MLD_{\sigma\theta}$ and MLD_{O2} (hereafter, $NCP_{\sigma\theta}$ and NCP_{O2}, respectively). In addition, we calculated a NCP_{30m} estimate based on a fixed 30-m MLD (MLD_{30m}) for direct comparisons with GPP_{30m} and NPP_{30m}.

The relatively shallow $MLD_{\sigma\theta}$ resulted in short O_2 residence time; hence, daily changes in wind affected NCP calculations most strongly

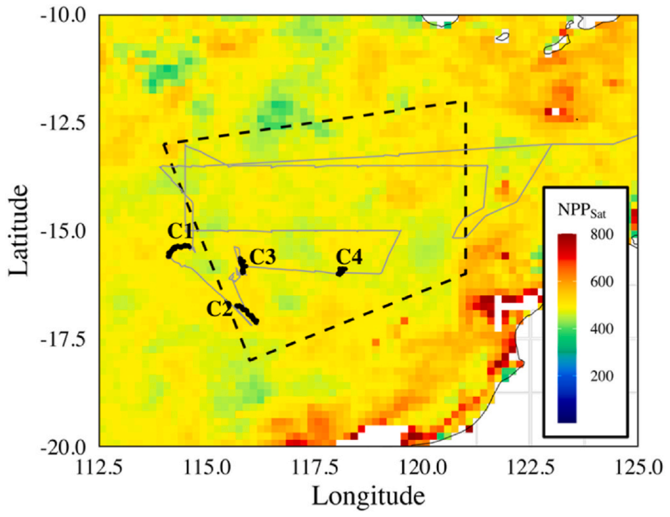

Fig. 4. Satellite observed net primary productivity (NPP_{Sat}). The underlying data are from the CAFÉ model extracted for Feb. 10–17. The cruise track is shown in grey, the different cycles are indicated in black and the polygon indicated the study region as analyzed by (Kehinde et al., 2023) bounded by coordinates: 13°S, 114°E; 18°S, 116°E; 16°S, 121°E; 12°S, 121°E).

(Fig. 7). C1 had the highest $NCP_{\sigma\theta}$ (Table S2), ranging from 116 to 388 mg C m^{-2} d^{-1} (Table 2), with a cycle mean of 268 ± 64 mg C m^{-2} d^{-1}. This is likely due to mixing from the previous storm event as well as the integration over a deeper mixed layer. NCP_{O2} and NCP_{30m} estimates for C1 were 398 ± 81 and 205 ± 29 mg C m^{-2} d^{-1}, respectively (Table 2, Fig. 7). C2 exhibited substantially lower $NCP_{\sigma\theta}$, NCP_{O2}, and NCP_{30m} estimates of 39 ± 7, 130 ± 27, and 115 ± 21 mg C m^{-2} d^{-1}, respectively. C3 displayed the lowest values of 13 ± 7 ($NCP_{\sigma\theta}$), 32 ± 15 (NCP_{O2}), and 47 ± 27 mg C m^{-2} d^{-1} (NCP_{30m}). In C4, the respective estimates were 29 ± 6, 78 ± 11, and 80 ± 12 mg C m^{-2} d^{-1}.

Across all cycles, NCP_{30m} and NPP_{30m} averaged 119 ± 20 and 212 ± 14 mg C m^{-2} d^{-1}, respectively, resulting in a mean NCP:NPP_{30m} ratio of ~0.56 (Table 1). These results suggest that just over half of net primary production was retained within the upper 30 m, with the remainder lost to community respiration or export.

2.6. *Photophysiology*

During C1, lower light in the upper 30 m (PAR_{30m} = 452 ± 8 μmol photons m^{-2} s^{-1}) yielded a moderate PSII efficiency (Fv/Fm = 0.26 ± 0.002) and a light-saturation irradiance of 334 ± 9 μmol photons m^{-2} s^{-1} (Fig. S3). Under these lower-light conditions, cells showed a larger antenna size (σ = 6.62 ± 0.07 nm^2), significantly greater than C2 and C3 ($p < 0.01$), and exhibited modest nonphotochemical quenching in the dark-adapted state (NSV = 2.89 ± 0.01). Electron transport through the photosystem II ($1/\tau_{es}$ = 1.25 ± 0.04 ms^{-1}) was moderate (Fig. S3). For C2, average light intensity (PAR_{30m}) was 598 ± 9 μmol photons m^{-2} s^{-1} with a low photosynthetic quantum yield (Fv/Fm = 0.19 ± 0.003, the lowest of all cycles ($p < 0.0001$) and high Ek (412 μmol photons m^{-2} s^{-1}). Antenna size was significantly reduced compared to C1 (σ = 5.08 ± 0.11 nm^2; $p < 0.001$), while nonphotochemical quenching in the dark-adapted state increased (4.52 ± 0.10; $p < 0.01$) (Fig. S3). The electron transport rate through the photosystem (1/τ) increased slightly (1.4 ± 0.1 ms^{-1}), consistent with accelerated electron turnover under photostress. C3, the continuation of C1, exhibited similar mean light intensity compared to C2 (559 ± 10 μmol photons m^{-2} s^{-1}), and showed elevated photochemical efficiency (Fv/Fm = 0.30 ± 0.002; $p < 0.01$ versus C1) and light-use efficiency at sub-saturating irradiance (α = 0.046 ± 0.001; $p < 0.001$) and lowest Ek (283 ± 10; $p < 0.01$ μmol photons m^{-2} s^{-1} versus C1 and C2). Both σ (5.84 ± 0.04 nm^2) and nonphotochemical quenching (2.40 ± 0.03) were low, and $1/\tau_{es}$ was lowest (0.95 ± 0.03 ms^{-1}; $p < 0.01$) (Fig. S3)., indicating optimal light capture and minimal energy dissipation under balanced light conditions. During C4, the average light intensity (PAR30m = 579 ± 10 μmol photons m^{-2} s^{-1}) was similar to C2 and C3, with moderate PSII efficiency (Fv/Fm = 0.23 ± 0.003). The light-saturation irradiance (Ek = 302 ± 14 μmol photons m^{-2} s^{-1}) was intermediate between C1 and C3. Antenna size (σ = 6.17 ± 0.08 nm^1) showed a moderate value, closer to that of C1, while nonphotochemical quenching (NSV = 3.36 ± 0.06) indicated a moderate energy dissipation capacity. Electron transport rate through the photosystem ($1/\tau_{es}$ = 1.40 ± 0.04 ms^{-1}) was similar to C2, suggesting comparable electron turnover rates under these intermediate conditions (Fig. S3).

3. Discussion

3.1. *General features of the Argo Basin*

Our study revealed warm surface temperature, a mostly shallow $MLD_{\sigma\theta}$ and near-complete depletion of nitrate in surface waters of the Argo Basin (Fig. 1). Remaining phosphorus of 0.06 μmol L^{-1} gave ratios of dissolved inorganic N:P well below Redfield. The nitracline was consistently between 70 and 81 m, similar to the 67–75 m DCM (Fig. 2E). Residual ammonium (~0.01 μmol L^{-1}; Fig. 2J) throughout the EZ was consistent with efficient N recycling. Residual silicate (Fig. 2I; ~1.9 μmol L^{-1}) and available P aligned with dominance of small cyanobacteria such as *Prochlorococcus* and low abundances of silicified phytoplankton, like diatoms (Yingling et al., This issue). Additionally, the deep nitrite maxima (Fig. 2G) and O_2 depletion near the DCM (Fig. S2 (Stukel et al., This issue); suggested enhanced nitrification and microbial respiration, potentially supporting microaerobic processes such as denitrification or anammox (Dore et al., 2002; Fawcett et al., 2015). Despite these nutrient features (Fig. 2) and high cellular Chl*a* in the lower EZ (Fig. S1; (Stukel et al., This issue), >50 % of total NPP occurred in the upper 50 m (Fig. 2), indicating light limitation at depth (Geider et al., 1997; Kana et al., 1997). This was also notable as cloud-suppressed NPP_{14C} during the first three days of C1 (Fig. 3A) and as substantially reduced phytoplankton growth rates from dilution experiments incubated in the lower EZ (Landry et al., 2025).

Together, these features illustrate a recycling-dominated system, where N availability restricts surface productivity, light limits subsurface productivity and recycling processes sustain much of the community's N demand. The persistent low N:P ratios suggest favorable conditions for diazotrophy (Landolfi et al., 2018; Louchard et al., 2023),

Table 2
Rates of productivity measurements and ratios. Only average values are presented in this table. Cycle day values are presented in Supplemental Table S2. Rates are expressed in mg C m^{-2} d^{-1}. Numbers in parenthesis denote standard error of the mean for the rates and error propagated errors for the ratios.

Cycle-Day	NPP_{Sat}	NPP_{14C} (full)	NPP_{14C} (30 m)	GPP (30m)	NCP (sigma)	NCP (O2)	NCP (30 m)	N_2 Fix (30)	N_2 Fix (full)	GPP: NPP (30m)	NCP:NPP (30 m)
Cycle 1	518 (1)	283 (72)	164 (20)	352 (23)	268 (64)	398 (81)	205 (29)			2.15 (0.3)	1.25 (0.21)
Cycle 2	447 (19)	542 (43)	230 (23)	345 (55)	39 (7)	130 (27)	115 (21)	32 (2)	79 (5)	1.50 (0.27)	0.50 (0.13)
Cycle 3	429 (1)	546 (53)	224 (33)	381 (80)	13 (7)	32 (15)	47 (27)	35 (5)	73 (9)	1.70 (0.41)	0.21 (0.12)
Cycle 4	457 (7)	496 (28)	240 (21)	302 (57)	29 (6)	78 (11)	80 (12)	34 (2)	67 (5)	1.26 (0.28)	0.33 (0.06)
average	459 (2)	460 (40)	212 (14)	345 (16)	97 (34)	174 (46)	119 (20)	34 (2)	72 (4)	1.63 (0.14)	0.56 (0.1)

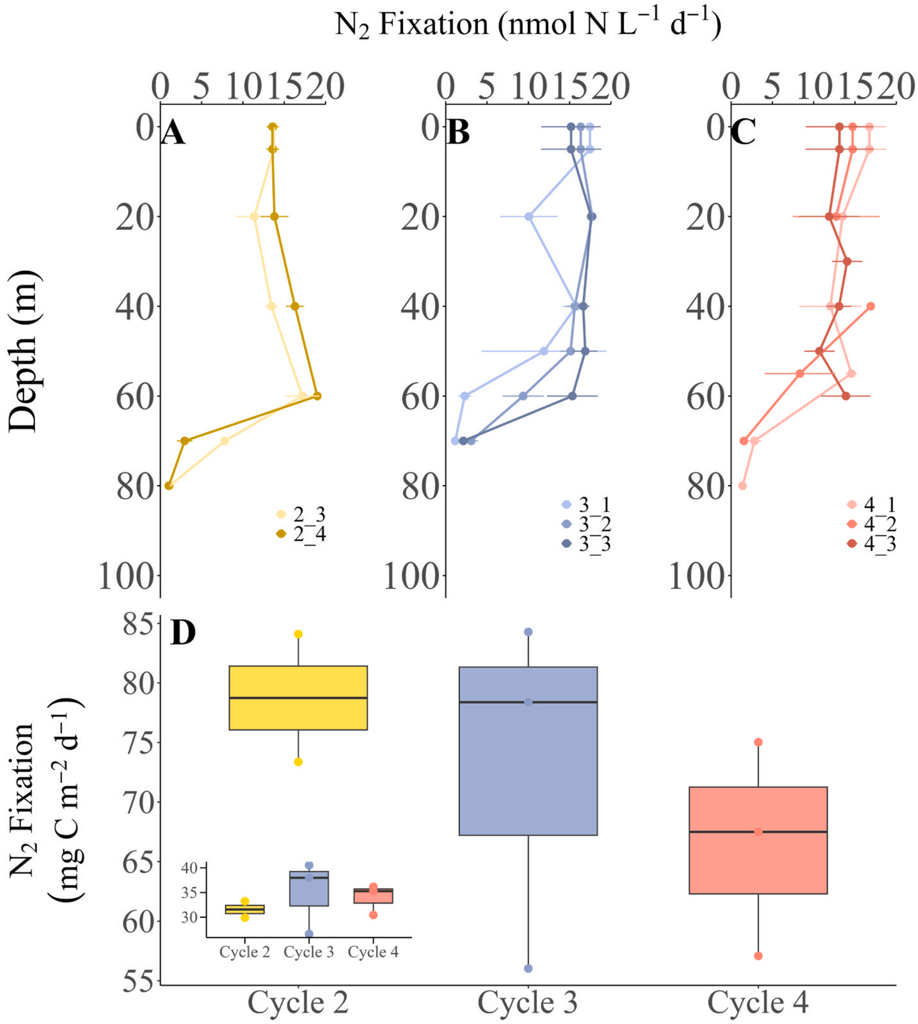

Fig. 5. N_2 fixation profiles and integrated rates. A-D); N_2-fixation over the depth of the array in nmol N m^{-3} d^{-1} for all cycles and cycle days. D) Integrated N_2-fixation in mg C m^{-2} d^{-1}. Dots indicate the water column integrated productivity for each day (n = 2, 3, 3 for Cycles 2, 3, and 4, respectively), while the boxplot indicates the median and interquartile range. Insert: Depth integrated N_2 fixation of the water column of the upper 30 m.

although the measured N_2 fixation rates (Fig. 5) and residual P suggest that diazotroph potential might not have been fully realized during our study period. In addition, Fe appears to be a co-limiting factor in cycles 1, 2 and 4 (pers. comm. Rob Lampe).

3.2. Net primary productivity

Our observed rates of NPP_{14C} are broadly consistent with long-term averages from oligotrophic gyres such as HOT and BATS (Brix et al., 2006), but 38 % higher than the mean estimate of 325 mg C m^{-2} d^{-1} for the Atlantic Bluefin Tuna spawning region in the Gulf of Mexico (Yingling et al., 2022). Productivity was highest in the upper 50 m, with subsurface productivity following decreasing light availability. The light-limiting nature of subsurface production was further supported by flow cytometric measurements showing increased cellular Chl*a* in *Prochlorococcus* and *Synechococcus* below 40 m (Fig. S1), as well as increases in Chl*a*:POC ratios below 50 m (Selph et al., This issue; Stukel et al., This issue). This pattern parallels previous observations from oligotrophic regions where DCMs are largely driven by pigment adjustments to low-light conditions (Mignot et al., 2014; Cornec et al., 2021; Phongphattarawat et al., 2023). DOC production (not measured) may add an additional 2–50 % to the NPP pool (Thornton, 2014). This would be especially significant in the nutrient-limited high-light section of the water column.

Comparing *in-situ* daily productivity (NPP_{14C}) to remotely sensed estimates using the 8-day composite CAFE model (NPP_{Sat}), NPP rates converged on similar cycle-averaged values of 460 mg C m^{-2} d^{-1} (Figs. 2 and 3, Table 1), supporting the general usage of such algorithms to assess productivity of this region. However, substantial discrepancies emerged on shorter timescales (Table S2, Figs. 3, 5 and 6). For instance, the day-to-day variability of NPP_{14C} in C1 (Fig. 2A) was not captured in the 8-day composite NPP_{Sat} assessment of productivity (Table S2), which remained stable throughout the observational period due to the longer time integration. Variability in NPP_{14C} reflects transient physical or biological processes such as short-term, changes in light availability and/or photoacclimation. Recognizing the fine-scale variability is crucial for understanding ecosystem dynamics in stratified environments, where productivity and community structure can shift on timescales of hours to days. While satellite algorithms have made progress in capturing depth-dependent distribution of biomass, Chl*a* and estimated productivity (Westberry et al., 2008), the inherent temporal and vertical differences impose a limited ability to resolve short-term changes in sub-surface production estimates in stratified oligotrophic systems, underscoring the continued importance of high-frequency *in-situ* observations.

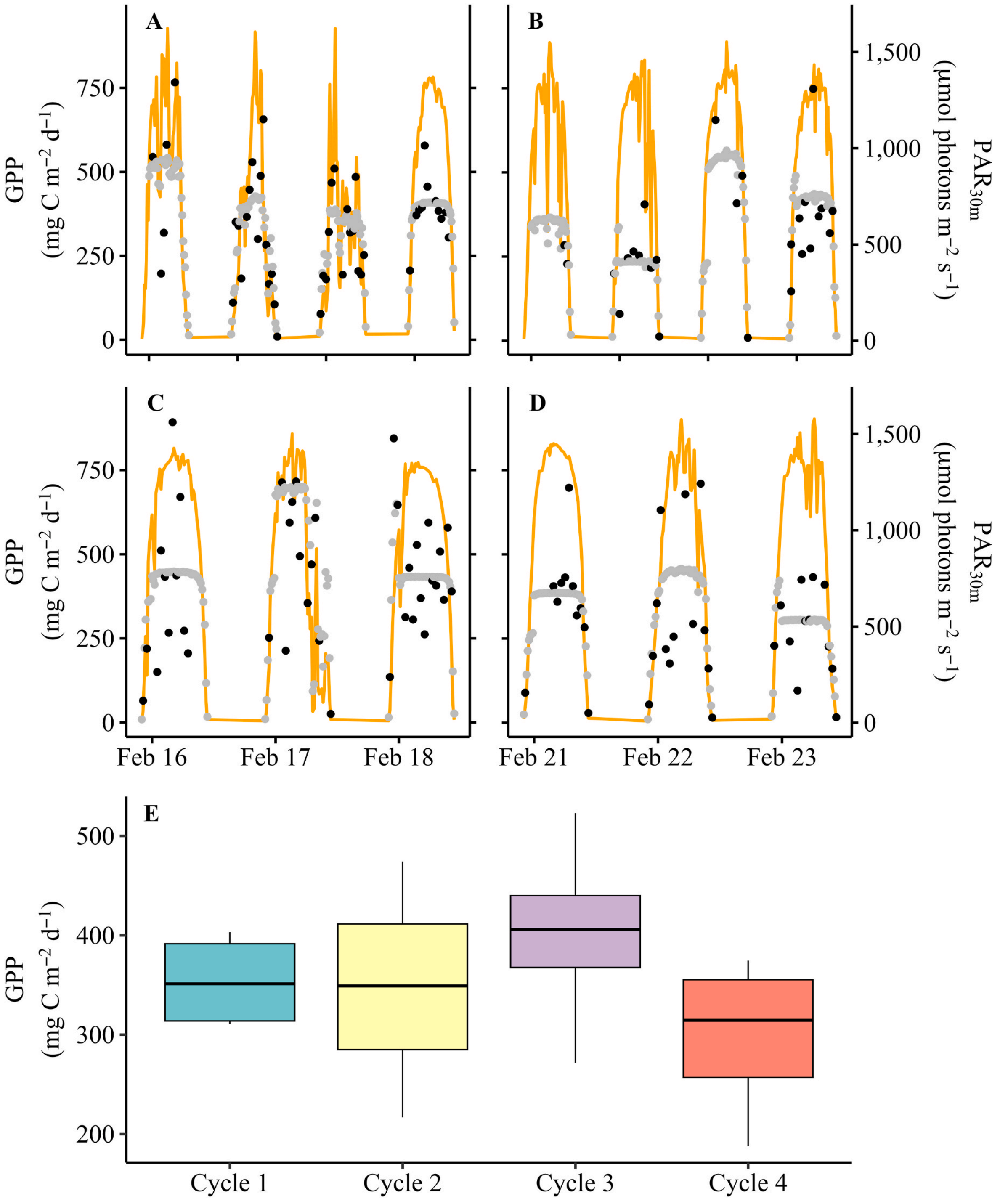

Fig. 6. Gross primary productivity over the diurnal cycles and integrated over 30 m. Panels A–D correspond to C1-C4, respectively. Orange lines indicate the median light intensity for 30 m water depth in µmol photons m^{-2} s^{-1}. Black dots indicate the calculated GPP for all valid FRRf P vs. E curves integrated over the upper 30 m. Grey dots indicate the interpolated data based on 30 min intervals using the average P vs. E (alpha, Pmax, beta) integrated over the upper 30 m. D: Average GPP for each cycle. (For interpretation of the references to color in this figure legend, the reader is referred to the Web version of this article.)

3.3. Support of NPP by N_2 fixation

N_2 fixation was estimated to be a secondary N source supporting primary production. As shown in Yingling et al. (This issue), ammonium utilization was the primary N source for the community while nitrate uptake was mostly negligible in surface waters. Using Redfield stoichiometry for C:N conversion, N_2-fixation rates for C2–C4 averaged 34 ± 2 mg C m^{-2} d^{-1} in the upper 30 m and 72 ± 4 mg C m^{-2} d^{-1} for the full profile (Fig. 5, Table 2) supporting16 % of measured NPP$_{14C}$. While Redfield stoichiometry provides a useful benchmark to convert N units to C units, oligotrophic systems do not universally follow Redfield. Systematic deviations in N:P and C:N with nutrient supply are well documented in central gyres (Galbraith and Martiny, 2015). However, since we do only have bulk C:N ratios and not phytoplankton-based assessment of C:N, Redfield stochiometry was the most realistic to apply to our data.

As such, N_2 fixation presents a substantial contribution to the “new” N pool in this region (Eppley and Peterson, 1979). More importantly for

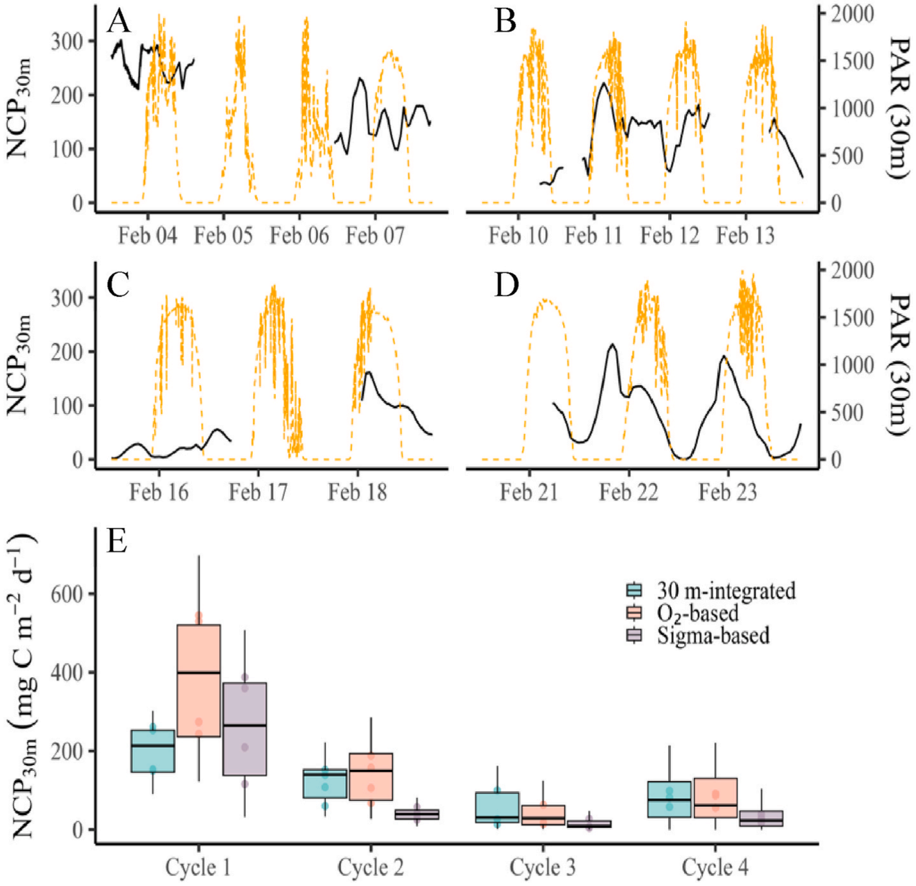

Fig. 7. Net Community Production (NCP, mg C m^{-2} d^{-1}) in each cycle. Panels A–D: Solar irradiance in orange; NCP calculated using MLD_{30m} in black over the day-night times for each cycle. E) NCP averaged over the cycle duration: Box plot indicates the calculations based on the different MLD applied (30-m integrated, O_2-based, or Sigma-based). (For interpretation of the references to color in this figure legend, the reader is referred to the Web version of this article.)

the biogeochemistry of this region, the N_2 fixation rates measured account for the majority of new N required to balance the measured carbon export of 18 % of NPP_{14C} into sediment traps (Stukel et al., this issue). In addition to our findings of the importance of N_2 fixation to export production in the Argo Basin, Radke et al. (2017) showed sediment organic matter with low $\delta^{15}N$ along he northwestern shelf region. This is an indication of organic matter produced supported by N_2 fixation in surface waters being exported. Similarly, Stukel et al. (this issue) analyzed $\delta^{15}N$ NO_3 during Cycle 4, the one closest to the shelf region. Elevated N_2 fixation rates were also measured closer to the shallower ITF (de Souza et al).

Complementary on-deck incubations performed on the cross-basin transects following C4 revealed more variable rates further in the central Argo Basin, and diel experiments (12 h daytime) indicated 2–3 fold higher daytime than nighttime rates. These rates would indicate that N_2-fixation by a mixture of photoautotrophic diazotrophs with different N_2 fixation strategies and/or heterotrophic diazotrophs contributed to the N budget in this region. Unicellular cyanobacterial diazotrophs (e.g., *Crocosphaera*) typically fix N_2 at night, utilizing daytime acquired carbon to generate the cellular energy needed for N_2 fixation (thus higher C requirements by day for night N fixation) (Mohr et al., 2010b; Zehr and Capone, 2020). In contrast, filamentous *Trichodesmium* fixes N_2 by day, using photosynthetic energy while employing O_2-protection strategies (Milligan et al., 2007; Kranz et al., 2010; Zehr and Capone, 2020). Both processes imply mechanistic linkages among light, cellular energy, reductant supply, and N_2-fixation rates and may be happening in our experiments.

Interestingly, residual phosphorus concentrations, low N:P ratios, warm temperature and strong stratification are considered diazotrophy-favorable conditions. Yet, the residual phosphorus also indicate that N_2 fixation was not fully realized. Ecological controls such as trace metal limitation and/or partial light limitation deeper in the water column may have constrained overall N fixation activity, as previously observed in other parts of the Indo-Pacific (Raes et al., 2015; Landolfi et al., 2018; Chowdhury et al., 2023).

3.4. *Gross production and autotrophic respiration*

Primary productivity involves the harvesting of light to split water, yielding energy and reductant for nutrient and carbon uptake and fixation (Falkowski, 2012). Variable fluorescence measurements quantify electron generation and transport rates through the photosystem. Carbon-based GPP estimates derived from FRRf measurements depend strongly on electrons used per carbon fixed (e:C) ratios, which can vary with species composition, light acclimation and nutrient status (Schuback et al., 2015, 2016; Boatman et al., 2019). In the present study, neither community composition (Yingling et al., This issue) nor nutrient status changed dramatically, and light availability was similar in C2 – C4 (but more limiting during C1). Hence, our cycle estimates should be reasonably comparable among themselves, but absolute values might be over- or underestimated (Halsey et al., 2013; Schuback et al., 2015; Boatman et al., 2019). A potential bias can be evaluated using the NPP: GPP ratios determined at 30 m. Assuming that GPP is theoretically 40–50 % greater than NPP (corresponding to an GPP/NPP ≈ 1.5 (Marra, 2002; Juranek and Quay, 2005), our results suggest that GPP may have been overestimated for the cruise average by ~9 % (average cycle deviations: C1: +43 %, C2: 0 %, C3: +13 %, C4: −16 %). This discrepancy is most likely attriuted to uncertainties in the electron-to-carbon conversion applied to the FRRf-derived measurements, reflecting variability in alternative electron transport pathways and in the cellular allocation of photosynthetically derived energy and reductants to metabolic processes other than carbon fixation.

Underway surface analysis from the ship's seawater intake ties the GPP estimates to the upper EZ, as both cellular pigmentation and photoacclimation dramatically change at greater depth. Based on flow cytometric data (Fig. S1), cellular Chla values were relatively stable to ~40 m but increased by 4–5 fold in the deeper EZ. GPP_{30m} rates of ~380 mg C m^{-2} d^{-1} were comparable to estimates for mid-to-offshore waters of the California Current Ecosystem (Kranz et al., 2020) but lower than the 440 and 710 mg C m^{-2} d^{-1} winter/summer estimates for station ALOHA based on oxygen isotope data (Juranek and Quay, 2005). However, because these rates were integrated over a deeper MLD (45–85 m) depth, our data seem to be within a generally expected range.

$GPP:NPP_{30m}$ ratios, using a 30-m integrated NPP_{14C} data subset, ranged between 0.67 and 3.2 with an average of 1.63 (Table 1). A ratio of ~1.63 is consistent with prior observations in oligotrophic regions where cellular respiration accounts for 40–70 % of gross photosynthesis (Laws et al., 2000; Marra and Barber, 2004; Halsey et al., 2013; Huang et al., 2021) with even higher % of respiration conducted by diazotrophic organisms (Kana, 1993; Milligan et al., 2007; Halsey et al., 2010; Kranz et al., 2010; Grosskopf and LaRoche, 2012). The higher GPP relative to NPP_{14C} highlights the substantial respiratory losses within the phytoplankton community and underscores the metabolic cost of maintaining growth under low-nutrient conditions (Halsey et al., 2010, 2013, 2014; Kranz et al., 2011; Eichner et al., 2014). Lower GPP_{30m} estimates compared to NPP_{30m} (observed C3, day 1 and C4, day 1) do, however, highlight some uncertainty of the FRRf method. Nonetheless, these GPP_{30m} estimates, when considered alongside NPP_{30m} and NCP_{30m} measurements, provide important constraints on trophic efficiency and organic carbon cycling in the region.

3.5. Community metabolism, new and export production using O_2/Ar analysis

In regions characterized by high regenerative productivity, such as the Argo Basin, the balance between NPP, NCP and export of particulate organic carbon (POC) is often assumed to approach a quasi-steady state where NCP approximates export production if no significant accumulation of organic matter occurs (Williams et al., 2004; Brix et al., 2006; Kranz et al., 2020). In oligotrophic systems, export production primarily reflects rapid sinking of zooplankton fecal pellets, enabling efficient vertical transfer of organic carbon despite generally low productivity (Stukel et al., This issue). This export relies on new production fueled by external N input, either via vertical supply of NO_3^- or biological N_2 fixation.

Our O_2:Ar-based NCP estimates were particularly sensitive to assumptions regarding MLD, which was very shallow based on σ_θ criteria. The more appropriate MLD assumptions (MLD_{O2} or the average of $MLD_{30\ m}$) resulted in mean NCP estimates of 174 and 119 mg C m^{-2} d^{-1}, respectively (Fig. 7, Table 2). In the following discussion, we primarily utilize NCP_{30m} estimates to compare water-column NCP rates to GPP and NPP measurements.

The elevated NCP observed during C1, leading to a NCP:NPP ratio above 1, is at odds with the theoretical assumption that NCP needs to be smaller than NPP. However, C1 was conducted just days after a storm event resulted in deep water-column mixing, causing potential entrainment of oxygen-rich upper DCM subsurface waters (Fig. S2), thus artificially elevating the O_2 concentration. Elevated NCP compared to NPP can be observed under certain physical forcings such as in upwelling regions (Kranz et al., 2020; Wang et al., 2020) or. as seen here, after a mixing event. The low O_2:Ar-derived NCP rates underscore the recycling-dominated nature of the Argo Basin. Export efficiencies (ratio of export to NPP), derived independently from sediment trap fluxes and NPP estimates, ranged from 0.085 to 0.23 (C1: 0.23, C2: 0.085, C3: 0.22, C3: 0.22; average: 0.18) (Stukel et al., This issue). These export ratios are notably higher than expected for a small-phytoplankton-dominated oligotrophic system (Buesseler and Boyd, 2009; Siegel et al., 2014; Karl et al., 2021; Stukel et al., 2024). Applying the average NPP_{14C} (460 mg C m^{-2} d^{-1}) and an export ratio of 0.18 yields an expected NCP of ~83 mg C m^{-2} d^{-1}, being reasonably close to our cycle-averaged NCP_{30m} values (Table 2, Fig. 6), but exceeding the estimates from C2–C4 by a factor of 2–3. The difference of NCP_{30m} compared to export estimates may partially reflect integration mismatches, as sediment trap fluxes were made just beneath the base of the EZ (116–127 m), while O_2/Ar estimates were constrained to a shallower mixed layer.

The positive NCP across the observation period further supports the net autotrophic status of the system, supplying organic matter to higher trophic levels which might be respired below the MLD_{O2}, as indicated by the strong negative O_2 gradient below the DCM (Supplemental Fig. S2). The continuously positive NCP also indicates that the system approached an ecosystem-wide metabolic balance during the period of measurement (Landry et al., 2025). In addition, since the Argo Basin expressed higher than expected NCP rates, it appears that higher trophic levels may effectively transfer energy through microbial and mesozooplankton food webs. This is supported by food-web analysis suggesting enhanced trophic transfer efficiencies (Landry et al., 2025).

3.6. Photophysiology

Analysis of the photosynthetic processes of electron generation and transport, energy dissipation and light-use efficiency can shed light on potential limitations of photoautotrophic productivity and the ability of cells to adjust to specific environmental conditions of the Argo Basin. During C1, reduced light availability following a transient mixing event resulted in moderate photosynthetic efficiency (Fv/Fm = 0.26) (Fig. S3A and B) and a light-saturation point (Ek) of ~334 μmol photons m^{-2} s^{-1} (Fig. S3 C). The phytoplankton community responded by increasing absorption cross section ($\sigma = 6.6$) (Fig. S3 E), indicative of a larger light-harvesting antennae to optimize photon capture under low light (MacIntyre et al., 2000; Falkowski and Raven, 2007). Non-photochemical quenching (NSV) remained modest (Fig. S3 F), indicating limited excess energy dissipation, while moderate electron turnover rates ($1/\tau$) (Fig. S3 G) suggested balanced excitation pressure and effective electron transport through the lower photosystem (Ruban, 2016). These photoacclimation responses helped to mitigate the reduction in primary productivity despite reduced irradiance, as reflected in the lowest NPP_{14C} observed during C1 (Westberry et al., 2008).

In contrast, higher light during C2 (PAR_{30m}–598 μmol photons m^{-2} s^{-1}) resulted in photophysiological signatures of photo-stress. The maximum photochemical efficiency of PSII (Fv/Fm) decreased significantly (0.19), while Ek increased to ~412 μmol photons m^{-2} s^{-1}, consistent with reduced photosynthetic efficiency at high light and or potential iron limitation (Behrenfeld and Milligan, 2013). The antenna size decreased significantly ($\sigma = 5$), suggesting contraction of light-harvesting structures to avoid overexcitation (Schuback et al., 2017). Elevated nonphotochemical quenching (NSV = 4.52) reflects enhanced energy dissipation to protect PSII from photodamage (Lavaud et al., 2016). The faster electron turnover ($1/\tau$) indicates increased electron cycling rates to dissipate excess excitation energy. These responses suggest that phytoplankton experienced physiological stress at higher irradiances but actively regulated energy input to maintain photochemical stability.

In C3, the continuation of C1, light levels remained moderately high (PAR_{30m}–559 μmol photons m^{-2} s^{-1}), and the data suggested a balanced light acclimation state. Fv/Fm increased to 0.30 (+0.04 compared to C1), the highest of all cycles, and light-utilization efficiency (α) was significantly elevated. The low Ek (~283 μmol photons m^{-2} s^{-1}), together with intermediate antenna size ($\sigma = 5.84$) and low non-photochemical quenching (NSV = 2.40), suggest optimal excitation balance under these more stable light conditions. The slower electron turnover ($1/\tau = 0.000953\ \mu s^{-1}$) reflects efficient energy conversion with minimal photoprotective dissipation. This optimized light utilization likely contributed to the relatively stable NPP_{14C} observed in C3 despite continued stratification.

During C4, light levels remained elevated (PAR_{30m}–579 μmol photons $m^{-2}\ s^{-1}$), but photophysiological responses indicated a transitional state between high-light stress and acclimation. Fv/Fm decreased to 0.23, suggesting mild photoinhibition and possible enhanced Fe stress, while Ek remained relatively low (~302 μmol photons $m^{-2}\ s^{-1}$), indicating incomplete acclimation to higher light. The antenna size (σ = 6.17), suggests a partial enhancement of light-harvesting complexes. Moderate non-photochemical quenching (NSV = 3.36) and rapid electron turnover rates ($1/\tau = 0.001397\ \mu s^{-1}$) indicate active photoprotective regulation and energy balancing to maintain efficient photosynthetic operation under fluctuating light and nutrient regimes.

Overall, these photophysiological patterns illustrated how the phytoplankton community employed flexible photoacclimation strategies to maintain productivity despite being nutrient and possibly Fe co-limited (Falkowski and Raven, 2007; Suggett et al., 2009). Under low light (C1), cells maximized light capture, while under high light (C2), cells minimized excess energy input and enhanced energy dissipation. The optimal balance achieved in C3 reflects a return to more stable stratified conditions, allowing efficient light utilization without the need for strong photoprotective responses. The transitional dynamics of C4 further highlight the community's capacity to fine-tune light harvesting and photoprotection in response to environmental shifts. These dynamic adjustments likely explain, in part, why overall primary productivity remained relatively stable across cycles, despite strong variability in surface irradiance. Flexible photoacclimation capacity is a key adaptation for phytoplankton communities inhabiting strongly stratified, oligotrophic systems such as the Argo Basin, where irradiance regimes can shift rapidly on sub-daily to multi-day timescales.

4. Conclusions

Across four Lagrangian experiments in the oligotrophic Argo Basin, NPP from ^{14}C and N_2-fixation *in-situ* incubation profiles and NPP satellite products, FRRf-derived GPP, and O_2/Ar-based NCP measurements offer a coherent view of the productivity regime, its variability and underlying metabolic processes. Satellite and ^{14}C measurements gave similar mean estimates (460 mg C $m^{-2}\ d^{-1}$) of NPP. A 1.7 GPP:NPP ratio for the upper 30 m was consistent with metabolic costs of growth under low-nutrient, high-light conditions. Below 50 m, light availability, rather than nutrients, was the primary limiting factor. N_2 fixation contributed ~16 % of NPP_{14C}, accounting for the new N required to balance high export rates in the system. The general agreement among approaches supports the robustness of our rate estimates, while also highlighting the strengths and caveats of different measurements. As climate warming continues to alter surface stratification, wind forcing and nutrient supply, these detailed measurements provide a baseline for assessing future changes in N utilization and productivity in this globally important tuna spawning region.

CRediT authorship contribution statement

Sven A. Kranz: Writing – review & editing, Writing – original draft, Visualization, Validation, Supervision, Resources, Project administration, Methodology, Investigation, Funding acquisition, Formal analysis, Data curation, Conceptualization. **Jared M. Rose:** Writing – review & editing, Validation, Investigation, Formal analysis, Data curation, Conceptualization. **Michael R. Stukel:** Writing – review & editing, Validation, Methodology, Investigation, Funding acquisition, Data curation, Conceptualization. **Karen E. Selph:** Writing – review & editing, Investigation, Funding acquisition, Formal analysis, Data curation, Conceptualization. **Natalia Yingling:** Writing – review & editing, Formal analysis. **Michael R. Landry:** Writing – review & editing, Validation, Project administration, Data curation, Conceptualization.

Declaration of competing interest

The authors declare that they have no known competing financial interests or personal relationships that could have appeared to influence the work reported in this paper.

Acknowledgements

We thank the captain and crew of the R/V Roger Revelle for their outstanding support and general assistance. Research support was provided by the National Science Foundation Grants OCE- 1851347 and 2404504 (to S.A.K.), OCE-1851381 (to K.E.S.), OCE-1851347 and OCE-1851558 (to M.R.L.), Seawater and plankton samples were collected under Australian Government permit AU-COM2021-520 and Australian Marine Parks permit PA2021-00062-2 issued by the Director of National Parks, Australia. The views expressed in this publication do not necessarily represent those of the Director of National Parks or the Australian Government.

Appendix A. Supplementary data

Supplementary data to this article can be found online at https://doi.org/10.1016/j.dsr2.2025.105570.

References

Behrenfeld, M.J., Falkowski, P.G., 1997. A consumer's guide to phytoplankton primary productivity models. Limnol. Oceanogr. 42, 1479–1491. https://doi.org/10.4319/lo.1997.42.7.1479.

Behrenfeld, M.J., Milligan, A.J., 2013. Photophysiological expressions of iron stress in phytoplankton. Ann. Rev. Mar. Sci 5, 217–246. https://doi.org/10.1146/annurev-marine-121211-172356.

Boatman, T.G., Geider, R.J., Oxborough, K., 2019. Improving the accuracy of single turnover active fluorometry (STAF) for the estimation of phytoplankton primary productivity (PhytoPP). Front. Mar. Sci. 6. https://doi.org/10.3389/fmars.2019.00319.

Brix, H., Gruber, N., Karl, D.M., Bates, N.R., 2006. On the relationships between primary, net community, and export production in subtropical gyres. Deep-Sea Res. Part II 53, 698–717. https://doi.org/10.1016/j.dsr2.2006.01.024.

Buesseler, K., Ball, L., Andrews, J., Benitez-Nelson, C., Belastock, R., Chai, F., Chao, Y., 1998. Upper ocean export of particulate organic carbon in the Arabian Sea derived from thorium-234. Deep-Sea Res. II 45, 2461–2487. https://doi.org/10.1016/S0967-0645(98)80022-2.

Buesseler, K.O., Boyd, P.W., 2009. Shedding light on processes that control particle export and flux attenuation in the twilight zone of the open ocean. Limnol. Oceanogr. 54, 1210–1232. https://doi.org/10.4319/lo.2009.54.4.1210.

Castro-Morales, K., Kaiser, J., 2012. Using dissolved oxygen concentrations to determine mixed layer depths in the bellingshausen sea. Ocean Sci. 8, 1–10. https://doi.org/10.5194/os-8-1-2012.

Chowdhury, S., Raes, E., Hörstmann, C., Ahmed, A., Ridame, C., Metzl, N., Bhavya, P.S., Sato, T., Shiozaki, T., Bonnet, S., Löscher, C.R., Singh, A., Benavides, M., 2023. Diazotrophy in the Indian Ocean: current understanding and future perspectives. Limnol. Oceanogr. Lett. 8, 707–722. https://doi.org/10.1002/lol2.10343.

Cornec, M., Claustre, H., Mignot, A., Guidi, L., Lacour, L., Poteau, A., D'Ortenzio, F., Gentili, B., Schmechtig, C., 2021. Deep chlorophyll maxima in the global ocean: occurrences, drivers and characteristics. Glob. Biogeochem. Cycles 35. https://doi.org/10.1029/2020GB006759.

Craig, H., Hayward, T., 1987. Oxygen supersaturation in the ocean - biological versus physical contributions. Science 235, 199–202. https://doi.org/10.1126/science.235.4785.199.

de Souza, A., Gu, S., Kranz, S.A., Rose, J., Lampe, R.H., Io, K.H., Deng, L., Liu, H., Landry, M.R., Cassar, N., This issue. Coastal hotspots of biological nitrogen fixation in an undersampled region of the eastern Indian Ocean. . Deep-Sea Res. II.,.

Desbruyères, D., McDonagh, E.L., King, B.A., Thierry, V., 2017. Global and full-depth ocean temperature trends during the early twenty-first century from argo and repeat hydrography. J. Clim. 30, 1985–1997. https://doi.org/10.1175/Jcli-D-17-0181.1.

Dore, J.E., Brum, J.R., Tupas, L.M., Karl, D.M., 2002. Seasonal and interannual variability in sources of nitrogen supporting export in the oligotrophic subtropical north Pacific Ocean. Limnol. Oceanogr. 47, 1595–1607. https://doi.org/10.4319/lo.2002.47.6.1595.

Dugdale, R.C., Goering, J.J., 1967. Uptake of new and regenerated forms of nitrogen in primary productivity. Limnol. Oceanogr. 12, 196–206. https://doi.org/10.4319/lo.1967.12.2.0196.

Eichner, M., Kranz, S.A., Rost, B., 2014. Combined effects of different CO_2 levels and N sources on the diazotrophic cyanobacterium *trichodesmium*. Physiol. Plantarum 152, 316–330. https://doi.org/10.1111/Ppl.12172.

Eppley, R.W., Peterson, B.J., 1979. Particulate Organic-Matter Flux and Planktonic New Production in the Deep Ocean. Nature 282, 677–680. https://doi.org/10.1038/282677a0.

Falkowski, P., 2012. Ocean science: the power of plankton. Nature 483, S17–S20. https://doi.org/10.1038/483S17a.

Falkowski, P.G., Raven, J.A., 2007. Aquatic Photosynthesis. Blackwell Publishers, Oxford.

Farley, J.H., Davis, T.L.O., 1998. Reproductive dynamics of southern bluefin tuna, *Thunnus maccoyii*. Fish. Bull. 96, 223–236.

Fawcett, S.E., Ward, B.B., Lomas, M.W., Sigman, D.M., 2015. Vertical decoupling of nitrate assimilation and nitrification in the Sargasso Sea. Deep-Sea Res., Part A I 103, 64–72. https://doi.org/10.1016/j.dsr.2015.05.004.

Field, C.B., Behrenfeld, M.J., Randerson, J.T., Falkowski, P., 1998. Primary production of the biosphere: integrating terrestrial and oceanic components. Science 281, 237–240. https://doi.org/10.1126/science.281.5374.237.

Galbraith, E.D., Martiny, A.C., 2015. A simple nutrient-dependence mechanism for predicting the stoichiometry of marine ecosystems. Proc. Natl. Acad. Sci. 112, 8199–8204. https://doi.org/10.1073/pnas.1423917112.

Geider, R.J., MacIntyre, H.L., Kana, T.M., 1997. Dynamic model of phytoplankton growth and acclimation: responses of the balanced growth rate and the chlorophyll a:carbon ratio to light, nutrient-limitation and temperature. Mar. Ecol. Prog. Ser. 148, 187–200. https://doi.org/10.3354/meps148187.

Grosskopf, T., LaRoche, J., 2012. Direct and indirect costs of dinitrogen fixation in *Crocosphaera watsonii* WH8501 and possible implications for the nitrogen cycle. Front. Microbiol. 3. https://doi.org/10.3389/fmicb.2012.00236.

Halsey, K.H., Milligan, A.J., Behrenfeld, M.J., 2010. Physiological optimization underlies growth rate-independent chlorophyll-specific gross and net primary production. Photosynth. Res. 103, 125–137. https://doi.org/10.1007/s11120-009-9526-z.

Halsey, K.H., Milligan, A.J., Behrenfeld, M.J., 2014. Contrasting strategies of photosynthetic energy utilization drive lifestyle strategies in ecologically important picoeukaryotes. Metabolites 4, 260–280. https://doi.org/10.3390/metabo4020260.

Halsey, K.H., O'Malley, R.T., Graff, J.R., Milligan, A.J., Behrenfeld, M.J., 2013. A common partitioning strategy for photosynthetic products in evolutionarily distinct phytoplankton species. New Phytol. 198, 1030–1038. https://doi.org/10.1111/nph.12209.

Hamme, R.C., Cassar, N., Lance, V.P., Vaillancourt, R.D., Bender, M.L., Strutton, P.G., Moore, T.S., DeGrandpre, M.D., Sabine, C.L., Ho, D.T., Hargreaves, B.R., 2012. Dissolved O_2/Ar and other methods reveal rapid changes in productivity during a Lagrangian experiment in the Southern Ocean. J. Geophys. Res., Oceans 117. https://doi.org/10.1029/2011jc007046.

Henson, S., Le Moigne, F., Giering, S., 2019. Drivers of carbon export efficiency in the global ocean. Glob. Biogeochem. Cycles 33, 891–903. https://doi.org/10.1029/2018gb006158.

Huang, Y., Nicholson, D., Huang, B., Cassar, N., 2021. Global estimates of marine gross primary production based on machine learning upscaling of field observations. Glob. Biogeochem. Cycles 35. https://doi.org/10.1029/2020GB006718 e2020GB006718.

Juranek, L.W., Quay, P.D., 2005. In vitro and in situ gross primary and net community production in the north Pacific subtropical gyre using labeled and natural abundance isotopes of dissolved O_2. Glob. Biogeochem. Cycles 19. https://doi.org/10.1029/2004gb002384.

Kana, T.M., 1993. Rapid oxygen cycling in *Trichodesmium thiebautii*. Limnol. Oceanogr. 38, 18–24. https://doi.org/10.4319/lo.1993.38.1.0018.

Kana, T.M., Geider, R.J., Critchley, C., 1997. Regulation of photosynthetic pigments in micro-algae by multiple environmental factors: a dynamic balance hypothesis. New Phytol. 137, 629–638. https://doi.org/10.1046/j.1469-8137.1997.00857.x.

Karl, D.M., Letelier, R.M., Bidigare, R.R., Björkman, K.M., Church, M.J., Dore, J.E., White, A.E., 2021. Seasonal-to-decadal scale variability in primary production and particulate matter export at Station ALOHA. Prog. Oceanogr. 195, 102563. https://doi.org/10.1016/j.pocean.2021.102563.

Kehinde, O., Bourassa, M., Kranz, S., Landry, M.R., Kelly, T., Stukel, M.R., 2023. Lateral advection of particulate organic matter in the eastern Indian Ocean. J. Geophys. Res., Oceans 128. https://doi.org/10.1029/2023JC019723.

Kolber, Z., Falkowski, P.G., 1993. Use of active fluorescence to estimate phytoplankton photosynthesis in-Situ. Limnol. Oceanogr. 38, 1646–1665. https://doi.org/10.4319/lo.1993.38.8.1646.

Kranz, S.A., Eichner, M., Rost, B., 2011. Interactions between CCM and N_2 fixation in *trichodesmium*. Photosynth. Res. 109, 73–84. https://doi.org/10.1007/S11120-010-9611-3.

Kranz, S.A., Levitan, O., Richter, K.-U., Prasil, O., Berman-Frank, I., Rost, B., 2010. Combined effects of CO_2 and light on the N_2-fixing cyanobacterium *trichodesmium* IMS101: physiological responses. Plant Physiol. 154, 334–345. https://doi.org/10.1104/pp.110.159145.

Kranz, S.A., Wang, S., Kelly, T.B., Stukel, M.R., Goericke, R., Landry, M.R., Cassar, N., 2020. Lagrangian studies of marine production: a multimethod assessment of productivity relationships in the California current ecosystem upwelling region. J. Geophys. Res., Oceans 125. https://doi.org/10.1029/2019JC015984.

Landolfi, A., Kähler, P., Koeve, W., Oschlies, A., 2018. Global marine N_2 fixation estimates: from observations to models. Front. Microbiol. 9. https://doi.org/10.3389/fmicb.2018.02112.

Landry, M.R., Laiz-Carrión, R., Kranz, S.A., Selph, K.E., Stukel, M.R., Malca, E., Die, D., Beckley, L.E., Décima, M., Swalethorp, R., Quintanilla, J.M., Yingling, N., Davies, C. H., Traboni, C., Borrego-Santos, R., Goes, J.I., deSouza, A., Romero-Fernández, P., Pennino, M.G., Kim, L.E., Kehinde, O., Lampe, R.H., Allen, A.E., Kelly, T.B., Muhling, B.A., Gu, S., Cassar, N., Laget, M., Biard, T., Liu, H., Io, K.H., Shiroza, A., Cawley, G., Fender, C.K., Rose, J.M., Jivanjee, A., Matisons, L., This issue. Overview of BLOOFINZ/INDITUN investigations of the southern bluefin spawning region off northwest Australia, january-march 2022. . Deep-Sea. Res. II.

Landry, M.R., Stukel, M.R., Yingling, N., Selph, K.E., Kranz, S.A., Fender, C.K., Swalethorp, R., Bhabu, R., 2025. Microbial food web dynamics in tropical waters of the bluefin tuna spawning region off northwestern Australia. Deep Sea Res. II. https://doi.org/10.1016/j.dsr2.2025.105547.

Lavaud, J., Six, C., Campbell, D.A., 2016. Photosystem II repair in marine diatoms with contrasting photophysiologies. Photosynth. Res. 127, 189–199. https://doi.org/10.1007/s11120-015-0172-3.

Laws, E.A., 1991. Photosynthetic quotients, new production and net community production in the open ocean. Deep-Sea Res., Part A A. 38, 143–167. https://doi.org/10.1016/0198-0149(91)90059-O.

Laws, E.A., Landry, M.R., Barber, R.T., Campbell, L., Dickson, M.L., Marra, J., 2000. Carbon cycling in primary production bottle incubations: inferences from grazing experiments and photosynthetic studies using ^{14}C and ^{18}O in the Arabian Sea. Deep-Sea Res. II 47, 1339–1352. https://doi.org/10.1016/S0967-0645(99)00146-0.

Lee, S.K., Park, W.S., Baringer, M.O., Gordon, A.L., Huber, B., Liu, Y.Y., 2015. Pacific origin of the abrupt increase in Indian Ocean heat content during the warming hiatus. Nat. Geosci. 8, 445–449. https://doi.org/10.1038/Ngeo2438.

Louchard, D., Münnich, M., Gruber, N., 2023. On the role of the amazon river for N_2 fixation in the Western tropical Atlantic. Glob. Biogeochem. Cycles 37. https://doi.org/10.1029/2022GB007537.

MacIntyre, H.L., Kana, T.M., Geider, R.J., 2000. The effect of water motion on short-term rates of photosynthesis by marine phytoplankton. Trend. Plant Sci. 5, 12–17. https://doi.org/10.1016/S1360-1385(99)01504-6.

Marra, J., 2002. Approaches to the measurement of plankton production. In: Williams, P. J.L., Thomas, D.N., Reynolds, C.S. (Eds.), Phytoplankton Productivity: Carbon Assimilation in Marine and Freshwater Ecosystems. Blackwell, Malden, Mass, pp. 78–108.

Marra, J., Barber, R.T., 2004. Phytoplankton and heterotrophic respiration in the surface layer of the ocean. Geophys. Res. Lett. 31. https://doi.org/10.1029/2004gl019664.

Mignot, A., Claustre, H., Uitz, J., Poteau, A., D'Ortenzio, F., Xing, X.G., 2014. Understanding the seasonal dynamics of phytoplankton biomass and the deep chlorophyll maximum in oligotrophic environments: a bio-argo float investigation. Glob. Biogeochem. Cycles 28, 856–876. https://doi.org/10.1002/2013gb004781.

Milligan, A.J., Berman-Frank, I., Gerchman, Y., Dismukes, G.C., Falkowski, P.G., 2007. Light-dependent oxygen consumption in nitrogen-fixing Cyanobacteria plays a key role in nitrogenase protection. J. Phycol. 43, 845–852. https://doi.org/10.1111/j.1529-8817.2007.00395.x.

Mohr, W., Grosskopf, T., Wallace, D.W.R., LaRoche, J., 2010a. Methodological underestimation of Oceanic nitrogen fixation rates. PLoS One 5. https://doi.org/10.1371/journal.pone.0012583.

Mohr, W., Intermaggio, M.P., LaRoche, J., 2010b. Diel rhythm of nitrogen and carbon metabolism in the unicellular, diazotrophic cyanobacterium Crocosphaera watsonii WH8501. Environ. Microbiol. 12, 412–421. https://doi.org/10.1111/J.1462-2920.2009.02078.X.

Morrow, R.M., Ohman, M.D., Goericke, R., Kelly, T.B., Stephens, B.M., Stukel, M.R., 2018. Cce V: primary production, mesozooplankton grazing, and the biological pump in the California current ecosystem: variability and response to El nino. Deep-Sea Res. I 140, 52–62. https://doi.org/10.1016/j.dsr.2018.07.012.

Oxborough, K., Moore, C.M., Suggett, D.J., Lawson, T., Chan, H.G., Geider, R.J., 2012. Direct estimation of functional PSII reaction center concentration and PSII electron flux on a volume basis: a new approach to the analysis of fast repetition rate fluorometry (FRRf) data. Lim Oce-Meth 10, 142–154. https://doi.org/10.4319/Lom.2012.10.142.

Phongphattarawat, S., Bouman, H.A., Lomas, M.W., Sathyendranath, S., Tarran, G.A., Ulloa, O., Zubkov, M.V., 2023. Ecophysiological basis of spatiotemporal patterns in picophytoplankton pigments in the global ocean. Front. Mar. Sci. 10. https://doi.org/10.3389/fmars.2023.1112177.

Platt, T., Gallegos, C.L., Harrison, W.G., 1980. Photoinhibition of Photosynthesis in Natural Assemblages of Marine-Phytoplankton. J. of Mar. Res. 38, 687–701.

Quay, P.D., Peacock, C., Bjorkman, K., Karl, D.M., 2010. Measuring primary production rates in the ocean: enigmatic results between incubation and non-incubation methods at station ALOHA. Glob. Biogeochem. Cycles 24. https://doi.org/10.1029/2009gb003665.

Radke, L., Nicholas, T., Thompson, P.A., Li, J., Raes, E., Carey, M., Atkinson, I., Huang, Z., Trafford, J., Nichol, S., 2017. Baseline biogeochemical data from Australia's continental margin links seabed sediments to water column characteristics. Mar. Freshw. Res. 68, 1593–1617. https://doi.org/10.1071/mf16219.

Raes, E.J., Thompson, P.A., McInnes, A.S., Nguyen, H.M., Hardman-Mountford, N., Waite, A.M., 2015. Sources of new nitrogen in the Indian Ocean. Glob. Biogeochem. Cycles 29, 1283–1297. https://doi.org/10.1002/2015gb005194.

Reuer, M.K., Barnett, B.A., Bender, M.L., Falkowski, P.G., Hendricks, M.B., 2007. New estimates of Southern Ocean biological production rates from O_2/Ar ratios and the triple isotope composition of O_2. Deep-Sea Res. I 54, 951–974. https://doi.org/10.1016/j.dsr.2007.02.007.

Robinson, C., Tilstone, G.H., Rees, A.P., Smyth, T.J., Fishwick, J.R., Tarran, G.A., Luz, B., Barkan, E., David, E., 2009. Comparison of in vitro and in situ plankton production determinations. Aquat. Microb. Ecol. 54, 13–34. https://doi.org/10.3354/ame01250.

Ruban, A.V., 2016. Nonphotochemical chlorophyll fluorescence quenching: mechanism and effectiveness in protecting plants from photodamage. Plant Physiol 170, 1903–1916. https://doi.org/10.1104/pp.15.01935.

Schuback, N., Flecken, M., Maldonado, M.T., Tortell, P.D., 2016. Diurnal variation in the coupling of photosynthetic electron transport and carbon fixation in iron-limited phytoplankton in the NE subarctic Pacific. Biogeosci 13, 1019–1035. https://doi.org/10.5194/bg-13-1019-2016.

Schuback, N., Hoppe, C.J.M., Tremblay, J.E., Maldonado, M.T., Tortell, P.D., 2017. Primary productivity and the coupling of photosynthetic electron transport and carbon fixation in the Arctic Ocean. Limnol. Oceanogr. 62, 898–921. https://doi.org/10.1002/lno.10475.

Schuback, N., Schallenberg, C., Duckham, C., Maldonado, M.T., Tortell, P.D., 2015. Interacting effects of light and iron availability on the coupling of photosynthetic electron transport and CO_2-Assimilation in marine phytoplankton. PLoS One 10. https://doi.org/10.1371/journal.pone.0133235.

Schuback, N., Tortell, P.D., 2019. Diurnal regulation of photosynthetic light absorption, electron transport and carbon fixation in two contrasting Oceanic environments. Biogeosciences 16, 1381–1399. https://doi.org/10.5194/bg-16-1381-2019.

Selph, K.E., Lampe, R.H., Yingling, N., Bhabu, R., Kranz, S.A., Allen, A.E., Landry, M.R., This issue. Phytoplankton community composition in the oligotrophic Argo basin of the eastern Indian Ocean. Deep-Sea Res. II,.

Siegel, D.A., Buesseler, K.O., Doney, S.C., Sailley, S.F., Behrenfeld, M.J., Boyd, P.W., 2014. Global assessment of ocean carbon export by combining satellite observations and food-web models. Glob. Biogeochem. Cycles 28, 181–196. https://doi.org/10.1002/2013gb004743.

Silsbe, G.M., Behrenfeld, M.J., Halsey, K.H., Milligan, A.J., Westberry, T.K., 2016. The CAFE model: a net production model for global ocean phytoplankton. Glob. Biogeochem. Cycles 30, 1756–1777.

Steemann Nielsen, E., 1952. The use of radio-active carbon ^{14}C for measuring organic production in the sea. ICES J. Mar. Sci. 18, 117–140.

Stukel, M.R., Biard, T., Décima, M., Fender, C.K., Kehinde, O., Kelly, T.B., Kranz, S.A., Laget, M., Landry, M.R., Yingling, N., This issue. Sinking particle export within and beneath the euphotic zone in the eastern Indian Ocean. Deep Sea Res. II,.

Stukel, M.R., Décima, M., Kelly, T.B., Landry, M.R., Nodder, S.D., Ohman, M.D., Selph, K. E., Yingling, N., 2024. Relationships between plankton size spectra, net primary production, and the biological carbon pump. Glob. Biogeochem. Cycles 38. https://doi.org/10.1029/2023GB007994.

Suggett, D.J., Stambler, N., Prasil, O., Kolber, Z., Quigg, A., Vazquez-Dominguez, E., Zohary, T., Berman, T., Iluz, D., Levitan, O., Lawson, T., Meeder, E., Lazar, B., Bar-Zeev, E., Medova, H., Berman-Frank, I., 2009. Nitrogen and phosphorus limitation of oceanic microbial growth during spring in the Gulf of Aqaba. Aquat. Microb. Ecol. 56, 227–239. https://doi.org/10.3354/Ame01357.

Tang, W.Y., Wang, S., Fonseca-Batista, D., Dehairs, F., Gifford, S., Gonzalez, A.G., Gallinari, M., Planquette, H., Sarthou, G., Cassar, N., 2019. Revisiting the distribution of oceanic N_2 fixation and estimating diazotrophic contribution to marine production. Nat. Commun. 10. https://doi.org/10.1038/s41467-019-08640-0.

Teeter, L., Hamme, R.C., Ianson, D., Bianucci, L., 2018. Accurate estimation of net community production from O-2/Ar measurements. Glob. Biogeochem. Cycles 32, 1163–1181. https://doi.org/10.1029/2017gb005874.

Thornton, D.C.O., 2014. Dissolved organic matter (DOM) release by phytoplankton in the contemporary and future ocean. Eur. J. Phycol. 49, 20–46. https://doi.org/10.1080/09670262.2013.875596.

Wang, S., Kranz, S.A., Kelly, T.B., Song, H., Stukel, M.R., Cassar, N., 2020. Lagrangian studies of net community production: the effect of Diel and multiday nonsteady state factors and vertical fluxes on O-2/Ar in a dynamic upwelling region. Geophys. Res. Bull. 125. https://doi.org/10.1029/2019JG005569.

Wanninkhof, R., 2014. Relationship between wind speed and gas exchange over the ocean revisited. Limnol Oceanogr. Methods 12, 351–362. https://doi.org/10.4319/lom.2014.12.351.

Webb, W.L., Newton, M., Starr, D., 1974. Carbon-dioxide exchange of alnus-rubra - Mathematical-Model. Oecologia 17, 281–291. https://doi.org/10.1007/Bf00345747.

Westberry, T., Behrenfeld, M.J., Siegel, D.A., Boss, E., 2008. Carbon-based primary productivity modeling with vertically resolved photoacclimation. Glob. Biogeochem. Cycles 22. https://doi.org/10.1029/2007gb003078.

White, A.E., Granger, J., Selden, C., Gradoville, M.R., Potts, L., Bourbonnais, A., Fulweiler, R.W., Knapp, A.N., Mohr, W., Moisander, P.H., Tobias, C.R., Caffin, M., Wilson, S.T., Benavides, M., Bonnet, S., Mulholland, M.R., Chang, B.N.X., 2020. A critical review of the N_2 tracer method to measure diazotrophic production in pelagic ecosystems. Limnol Oceanogr. Methods 18, 129–147. https://doi.org/10.1002/lom3.10353.

Williams, P.J.L., Morris, P.J., Karl, D.M., 2004. Net community production and metabolic balance at the oligotrophic ocean site, station ALOHA. Deep-Sea Res. I 51, 1563–1578. https://doi.org/10.1016/j.dsr.2004.07.001.

Yingling, N., Kelly, T.B., Shropshire, T.A., Landry, M.R., Selph, K.E., Knapp, A.N., Kranz, S.A., Stukel, M.R., 2022. Taxon-specific phytoplankton growth, nutrient utilization and light limitation in the oligotrophic Gulf of Mexico. J. Plankton Res. 44, 656–676. https://doi.org/10.1093/plankt/fbab028.

Yingling, N., Selph, K.E., Landry, M.R., Kranz, S.A., Johnson, M., Stukel, M.R., This issue. Phytoplankton nutrient uptake, community composition and biomass in the eastern Indian Ocean off northwest Australia. Deep-Sea Res. II.

Zehr, J.P., Capone, D.G., 2020. Changing perspectives in marine nitrogen fixation. Science 368. https://doi.org/10.1126/science.aay9514.